JGR Earth Surface

RESEARCH ARTICLE

10.1029/2021JF006422

Key Points:

- A delta experiment shows sea-level rise causes more frequent avulsions at a constant distance upstream of the river mouth
- During sea-level fall, avulsions occur if progradation into the offshore basin is fast enough to counteract incision and cause aggradation
- In stratigraphy, avulsion-induced incision overprints sea-level scours smaller than the channel depth or greater than the basin depth

Supporting Information:

Supporting Information may be found in the online version of this article.

Correspondence to:

A. J. Chadwick,
austin.chadwick23@gmail.com

Citation:

Chadwick, A. J., Steele, S., Silvestre, J., & Lamb, M. P. (2022). Effect of sea-level change on river avulsions and stratigraphy for an experimental lowland delta. *Journal of Geophysical Research: Earth Surface*, *127*, e2021JF006422. https://doi.org/10.1029/2021JF006422

Received 7 SEP 2021
Accepted 24 JUN 2022

Author Contributions:

Conceptualization: A. J. Chadwick, M. P. Lamb
Funding acquisition: A. J. Chadwick, M. P. Lamb
Investigation: A. J. Chadwick, S. Steele, J. Silvestre, M. P. Lamb
Supervision: A. J. Chadwick, M. P. Lamb
Writing – review & editing: A. J. Chadwick, S. Steele, J. Silvestre, M. P. Lamb

Effect of Sea-Level Change on River Avulsions and Stratigraphy for an Experimental Lowland Delta

A. J. Chadwick[1], S. Steele[1], J. Silvestre[1], and M. P. Lamb[1]

[1]Division of Geological and Planetary Sciences, California Institute of Technology, Pasadena, CA, USA

Abstract Lowland deltas experience natural diversions in river course known as avulsions. River avulsions pose catastrophic flood hazards and redistribute sediment that is vital for sustaining land in the face of sea-level rise. Avulsions also affect deltaic stratigraphic architecture and the preservation of sea-level cycles in the sedimentary record. Here, we present results from an experimental lowland delta with persistent backwater effects and systematic changes in the rates of sea-level rise and fall. River avulsions repeatedly occurred where and when the river aggraded to a height of nearly half the channel depth, giving rise to a preferential avulsion node within the backwater zone regardless of sea-level change. As sea-level rise accelerated, the river responded by avulsing more frequently until reaching a maximum frequency limited by the upstream sediment supply. Experimental results support recent models, field observations, and experiments, and suggest anthropogenic sea-level rise will introduce more frequent avulsion hazards farther inland than observed in recent history. The experiment also demonstrated that avulsions can occur during sea-level fall—even within the confines of an incised valley—provided the offshore basin is shallow enough to allow the shoreline to prograde and the river to aggrade. Avulsions create erosional surfaces within stratigraphy that bound beds reflecting the amount of deposition between avulsions. Avulsion-induced scours overprint erosional surfaces from sea-level fall, except when the cumulative drop in sea-level is greater than the channel depth and less than the basin depth. Results imply sea-level signals outside this range are removed or distorted in delta deposits.

Plain Language Summary Rivers on deltas are unstable and naturally change course every ~10–1,000 years through a process known as avulsion. Avulsions are responsible for some of the deadliest natural disasters in human history and for depositing sediment that builds sedimentary records and sustains coastal landscapes in the face of anthropogenic sea-level rise. Sea level can affect where and when channels shift course, but understanding these effects is difficult because avulsions occur infrequently. Here, we present findings from a laboratory experiment that produced avulsions on a delta in miniature. As sea level rises more quickly, we found that avulsions occur more often and at locations farther upstream. The record of avulsions is recorded in the pattern of sedimentary layers within the delta, but this pattern may be confused with erosion during sea-level fall. Findings from this experiment support recent predictions and observations of deltas in nature.

1. Introduction

River deltas are home to diverse ecosystems, valuable resources, and nearly half a billion of the human population (Gleick, 2003; Olson & Dinerstein, 1998; Vörösmarty et al., 2009). Many deltas develop a triangular-shaped planform morphology through natural diversions in channel course to the shoreline, known as river avulsions, which occur periodically every ~10 – 1000 years depending on the delta (Figures 1a and 1b) (Slingerland & Smith, 2004). Avulsions are a hazard to human life and property (Sinha, 2009; Syvitski & Brakenridge, 2013) and have been responsible for some of the deadliest flood disasters in human history (Kidder & Liu, 2017; Soong & Zhao, 1994). At the same time, avulsions are necessary to counter land lost by nourishing subsiding wetlands with sediment, nutrients, and carbon (Figure 1b) (Edmonds et al., 2009; Richards et al., 2002). Anthropogenic interference and greenhouse effects are contributing to relative sea-level rise across the globe (Pachauri et al., 2014), and engineered avulsions are important elements of billion-dollar coastal restoration plans to combat rise and sustain coastal cities and ecosystems (Brakenridge et al., 2017; Coastal Protection and Restoration Authority of Louisiana, 2007). To increase the success of such plans, we need to understand where and when river avulsions naturally occur on deltas.

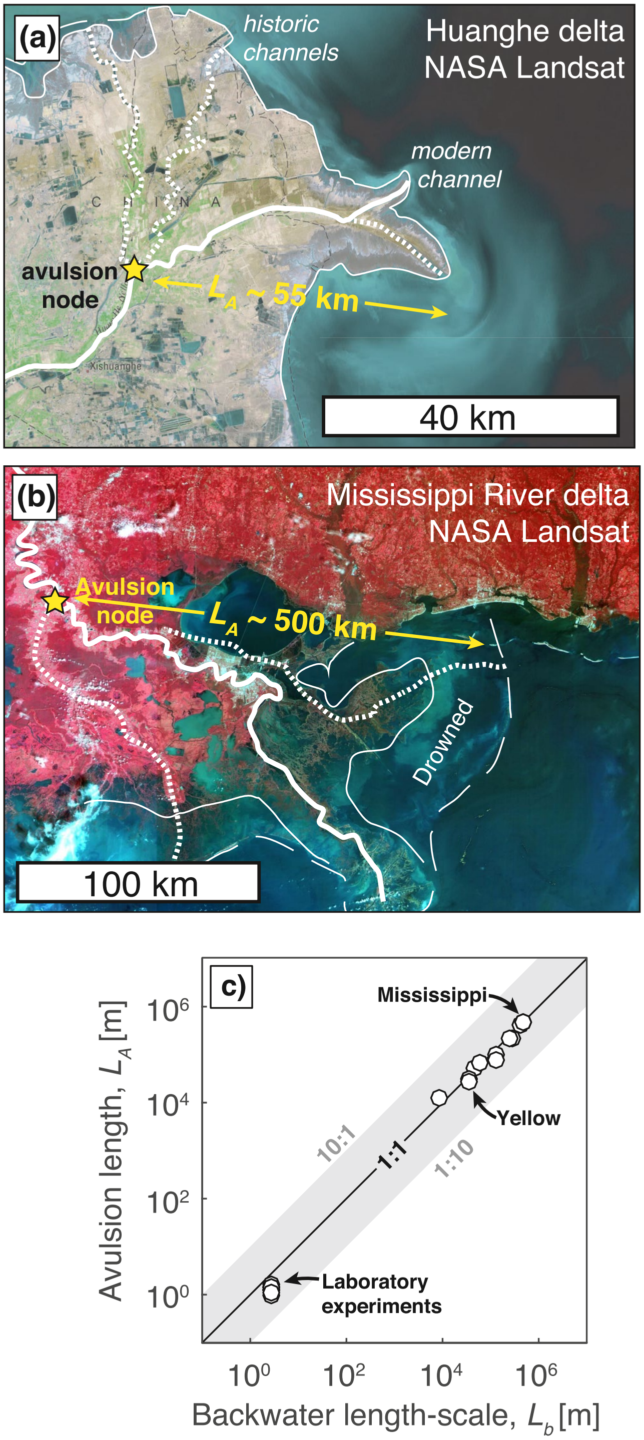

Figure 1. (a) Huanghe delta, China, illustrating modern (solid line) and abandoned (dotted line) channel pathways and avulsion node (yellow star). (b) Mississippi River delta, USA. Thin dashed line indicates approximate shoreline in 1900 A.D. (Gagliano et al., 1981). (c) Correlation between measured avulsion length and computed backwater length-scale (Equation 1), which approximates the length of the backwater zone where sea level causes gradually varied flow (Chatanantavet et al., 2012; Jerolmack & Swenson, 2007).

Interpreting ancient delta deposits depends in part on our ability to disentangle stratigraphic patterns of sea-level change and river avulsions. Fluviodeltaic deposits are major building blocks of the sedimentary record on Earth, and are important reservoirs of hydrocarbon and freshwater resources (Bohacs & Suter, 1997; Hariharan et al., 2021). On Mars, the Perseverance rover has begun exploration of ancient deltaic deposits to unravel lake-level history and assess conditions for ancient life (Farley et al., 2020). Repeating sequences in sedimentary strata are thought to generally reflect changes in sea level over time, with deposition during sea-level rise and erosion during sea-level fall (i.e., sequence stratigraphy) (Allen & Posamentier, 1993; Van Wagoner, 1998). However, deciphering this record is not always clear: avulsions and floods can create erosional surfaces, regardless of sea-level change, which appear similar to scour generated during sea-level fall (Ganti et al., 2019; Trower et al., 2018). In addition, deposition can occur during sea-level fall if sediment supply and basin geometry allow for rapid shoreline progradation (Bijkerk et al., 2016; Wang et al., 2019) or if the river is temporarily disconnected with the shelf edge (Van Heijst & Postma, 2001).

Global compilations of lowland river deltas show avulsions preferentially occur at a relatively fixed location, termed the avulsion node (Figures 1a and 1b). The avulsion node is found at a distance upstream of the shoreline that scales with the backwater length-scale,

$$L_A \propto L_b \tag{1}$$

where L_A is the avulsion length measured along the channel from the river mouth to the avulsion location, and L_b is the backwater length-scale, defined as the ratio of channel depth, H_c, to average bed slope, S (i.e., $L_b = H_c/S$; Figure 1c) (Chatanantavet et al., 2012; Jerolmack & Swenson, 2007). The backwater length-scale approximates the river reach where sea level influences river hydraulics—termed the backwater zone—which extends for hundreds of kilometers for large, low-sloping rivers (Lamb et al., 2012; Paola & Mohrig, 1996). Deltas exhibiting this scaling are referred to as backwater-scaled deltas. In this study, we focus on backwater-scaled deltas and the regional backwater effects that can span entire deltas, rather than smaller scale backwater effects that can influence more local sedimentation processes (Shaw & McElroy, 2016; Van Dijk et al., 2012).

Recent models have reproduced backwater-scaled deltas (cf. Chatanantavet et al., 2012; Moodie et al., 2019; Wu & Nitterour, 2020). Simulations show cycles of low flows and high flows in the backwater zone are responsible for creating a spatial maximum in deposition that determines the avulsion site (Chadwick et al., 2019; Chatanantavet et al., 2012). Models predict sea-level rise does not affect the avulsion length (L_A), but could induce higher aggradation rates at the avulsion node, resulting in more frequent avulsions (Chadwick et al., 2020; Ratliff et al., 2018). Avulsion frequency is expected to increase when sea-level rise is comparable to the aggradation rate; in this regime, sea-level rise facilitates faster delta-top aggradation and stifles delta-front progradation. At slower rise rates, avulsion frequency is unaffected because aggradation associated with progradation outpaces the effect of sea-level rise. At much higher rise rates, there is simply not enough sediment to keep pace with sea level; progradation ceases, channels aggrade as fast as possible given the sediment input, and avulsion frequency reaches a maximum. Avulsions may cease altogether if the delta drowns (Chadwick et al., 2020; Wu & Nitterour, 2020) or if offshore basin geometry hinders aggradation (Bijkerk et al., 2016; Wang et al., 2019). Avulsions typically take decades to centuries or longer to occur in nature, so direct observations that test these predictions are sparse.

Experimental studies offer an opportunity to observe repeated avulsions at reduced scale. Hypotheses can be tested under controlled, simplified conditions, often reducing the complexity associated with vegetation, cohesive floodplains, offshore waves and tides, and other factors capable of influencing individual avulsions in nature (Finotello et al., 2019; Nicholas et al., 2018; Piliouras & Kim, 2019). Generally, experiments have demonstrated that avulsions are associated with cycles of local shoreline progradation and lobe construction (de Haas et al., 2016; Reitz et al., 2010; Van Dijk et al., 2012). However, until recently, most experiments featured relatively steep surface slopes, braided rivers, and minimal backwater effects (cf. Muto & Steel, 2004; Reitz & Jerolmack, 2012; Wickert et al., 2013), producing hydrodynamics and sediment transport more akin to alluvial fans and fan deltas than they are to lowland, backwater-influenced deltas (Ganti et al., 2014). In a pioneering experiment, Hoyal and Sheets (2009) utilized a constant input water discharge and cohesive sediment mixture that naturally produced gentle slopes and single-thread channels. Avulsion in their experiment was caused by shoreline progradation: as the shoreline advanced seaward, the river profile lengthened and its slope declined, leading to a reduction in sediment transport capacity that promoted aggradation and avulsion. Later experiments and models supported and expanded upon this finding, demonstrating that progradation—as well as relative sea-level rise—ultimately set the pace of aggradation and avulsion on lowland deltas (Martin et al., 2009; Moodie et al., 2019; Yu et al., 2017).

Although progradation may set the pace of avulsion, it does not necessarily control where avulsion takes place. In the experiments of Hoyal and Sheets (2009), avulsion location coincided with weak points in the levee profile that allowed for maximum fluid shear stress during overbank flows, which could manifest at the scale of the backwater length (Edmonds et al., 2009; Hoyal & Sheets, 2009). Later models reproduced similar behavior (Chadwick et al., 2019; Ratliff et al., 2021), showing that for deltas subjected to a constant water discharge, the levee and floodplain topography is a dominant control on avulsion location. Levee and floodplain topography are sensitive to basin boundary and initial conditions (Pierik et al., 2017); avulsions are prone to occur where the basin enforces a downstream increase in levee and floodplain width or decrease in floodplain slope (Prasojo et al., 2022; Ratliff et al., 2021). However, in the absence of external forces and with a constant water discharge, levee and floodplain topography can equilibrate to a state where avulsions have a similar likelihood everywhere along the river profile (Chadwick et al., 2019). In contrast, major avulsions on natural deltas tend to occur at or near the delta-apex, which in turn tends to scale with the backwater length (Equation 1).

Avulsion location in nature is thought to originate from variable flow regimes that produce persistent sedimentation patterns in the backwater zone (Chadwick et al., 2019; Chatanantavet et al., 2012), but few experiments have been conducted under such conditions. Chatanantavet and Lamb (2014) conducted one such lowland river experiment with subcritical flows and a variable flood regime; in their experiment, backwater effects caused a downstream migrating wave of aggradation during low flows, and an upstream migrating wave of incision during high flows. Over many flow events, this interplay resulted in a spatial maximum in aggradation in the upstream part of the backwater zone. This finding was reproduced in a later experiment that utilized a larger facility allowing for repeated river avulsions (Ganti, Chadwick, Hassenruck-Guidpati, Fuller, & Lamb, 2016; Ganti, Chadwick, Hassenruck-Gudipati, & Lamb, 2016). Results demonstrated the spatial maximum in aggradation rate coincided with the avulsion node, leading to the emergence of a backwater-scaled avulsion length (Equation 1; Figure 1c). Importantly, backwater-scaled aggradation and avulsion were only reproduced in the presence of a variable flood regime; in a comparison experiment without floods, backwater-scaled avulsions did not occur (Ganti, Chadwick, Hassenruck-Guidpati, Fuller, & Lamb, 2016). These experimental investigations have supported numerical modeling efforts of deltas in nature (Chatanantavet et al., 2012; Moodie et al., 2019), but did not explore the effects of sea-level rise and fall on river avulsion patterns.

Here, we build on this recent experimental work (Chatanantavet & Lamb, 2014; Ganti, Chadwick, Hassenruck-Gudipati, Fuller, & Lamb, 2016; Ganti, Chadwick, Hassenruck-Gudipati, & Lamb, 2016) and present results from a backwater-scaled lowland delta experiment subjected to systematic sea-level rise and fall. First, we provide an overview of experimental design, scaling, and methods. Second, we present a walkthrough of experimental results for different sea-level conditions. Third, we use experimental data to test models of river-delta avulsion location and frequency, and compare the erosional signatures of avulsions and sea-level change preserved in

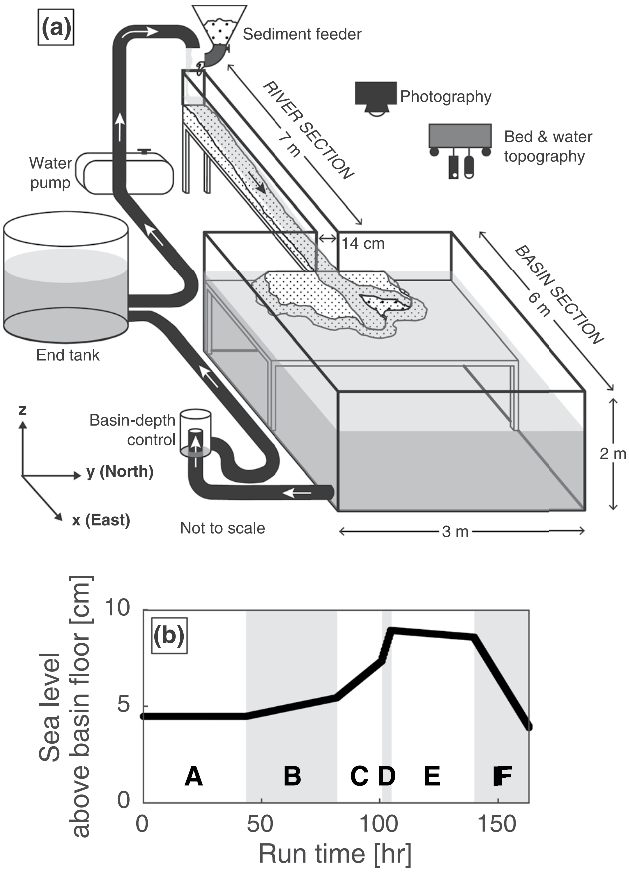

Figure 2. (a) Schematic of the Caltech River-Ocean Facility. The tank coordinate system was defined such that the primary flow direction was eastward. (b) Sea level as a function of run time over the course of the experiment. Alternate background shading indicates Phases A through F, each of which featured a different rate of sea-level change.

Table 1
Variable Flood Regime of the CROF18 Experiment

	Low flow	High flow
Water discharge[liters/min]	14.4	20.4
Sediment supply [g/min]	30.4	69.4
Normal-flow depth, H_n[mm]	7.5	11.7
Flow duration, T_{flow} [min]	22	8
Channel-adjustment timescale, T_{adj} [min]	45	20
Normal-flow transport slope, $S[-]$	0.0042	0.0042
Backwater length-scale*, $L_b = H_n/S$ [m]	1.8	–
Froude number, Fr [-]	0.59	0.43
Reynolds number, Re [-]	1,200	1,700
Shields number, τ^* [-]	0.18	0.28

*The backwater length-scale well approximates the length of the backwater zone but can be more accurately constrained by accounting for Fr and variable discharges (Equation 3) (Bresse, 1860; Lamb et al., 2012).

delta stratigraphy. Finally, we discuss implications for predicting future avulsion hazards on densely populated deltas and for interpreting the deposits of ancient deltas on Earth and Mars.

2. Materials and Methods

2.1. Experimental Design

We conducted a laboratory flume experiment called CROF18 in the Caltech River-Ocean Facility, the same facility used by Ganti, Chadwick, Hassenruck-Gudipati, Fuller, and Lamb (2016), Ganti, Chadwick, Hassenruck-Gudipati, and Lamb (2016); their experiment is referred to as CROF16. The experimental flume consisted of a 7-m-long, 14-cm-wide fixed-width river section that flowed into a 5-m-long, 3-m-wide unconfined ocean basin (Figure 2). Water and sediment were supplied at the upstream end, and sea level was controlled using a programmable standpipe at the downstream end. The basin was initially free of sediment, and over several hours the flow naturally deposited sediment to form an alluvial river and delta. We widened the width of the fixed walls in the river section (14 cm) compared to CROF16 (7 cm) to match the width of naturally formed channels on the delta top, in order to mitigate flow expansion and associated avulsion at the river-basin boundary. Further details regarding the experimental facility can be found in Ganti, Chadwick, Hassenruck-Gudipati, and Lamb (2016).

The CROF18 experiment was designed to simulate the simplest possible scenario that could reproduce backwater-scaled avulsions under changing sea level. We intentionally excluded complexities associated with cohesive sediment, floodplains, vegetation, waves, tides, and anthropogenic modification (Brakenridge et al., 2017; Caldwell & Edmonds, 2014; Finotello et al., 2019; Nicholas et al., 2018). These factors can influence avulsions in nature (cf. Piliouras & Kim, 2019; Ratliff et al., 2021), but previous modeling and simplified experiments suggest they are not necessary to reproduce backwater-scaled avulsion patterns to first order (Chadwick et al., 2019, Ganti, Chadwick, Hassenruck-Gudipati, Fuller, & Lamb, 2016) (Figure 1c). To produce a laboratory-scale river with similarities to natural lowland rivers, we selected water discharges such that flow was subcritical ($Fr < 1$) and turbulent ($Re > 1000$) (Table 1) (Kleinhans et al., 2014, 2015; Paola et al., 2009). To achieve sediment transport at such low discharges, we used low-density sediment: crushed, non-cohesive walnut shells (1300 $\mathrm{kg/m^3}$) with near-uniform particle diameter (0.7 mm). This sediment mixture yielded a normal-flow Shields number that was similar to channels in nature ($\tau^* \sim 0.2$; Table 1) and that was high enough to avoid current ripples and associated scour holes in the laboratory (Kleinhans et al., 2017). Non-cohesive sediment is sufficient to produce avulsions and stratigraphy similar to natural avulsive systems (Paola et al., 2009; Straub et al., 2012), though we note that channel lateral migration and channel geometry can exhibit differences compared to lowland river channels in nature with cohesive, vegetated banks (Dunne & Jerolmack, 2020; Tal & Paola, 2007).

To reproduce laboratory-scale backwater zones, we implemented a variable flood regime following the example of CROF16. Water and sediment supply oscillated between a low-flow and high-flow discharge (Table 1). Water discharges associated with each flow were selected to produce significantly different normal flow depths (7.5 mm during low flows and 11.7 mm during high flows, a ~40% difference) to facilitate significant changes in water-surface slope as flow approached sea level in the backwater zone (Chatanantavet et al., 2012). Furthermore, the durations for each flow

Table 2
Phases of the CROF18 Experiment and Associated Sea-Level Change

	Phase A	Phase B	Phase C	Phase D	Phase E	Phase F
Dimensionless sea-level rise rate, σ^* [−]	0	0.08	0.33	1.33	−0.03	−0.67
Sea-level rise rate, σ $\left[\frac{\text{mm}}{\text{hr}}\right]$	0	0.25	1	4	−0.1	−2
Run time [hr]	0–43.5	43.5–82	82–101	101–105	105–140	140–163.5
Duration, [hr]	43.5	38.5	19	4	35	23.5
Number of low flows [-]	87	77	38	8	70	47
Number of high flows [-]	87	77	38	8	70	47

($T_{flow} = 22$ min for low flows, $T_{flow} = 8$ min for high flows) were selected to be significantly shorter than the time required to adjust the backwater zone to uniform-flow conditions (~45 min for low flow, ~20 min for high flow) estimated using the channel-adjustment timescale, $T_{adj} = \frac{L_b B_c \Delta H}{Q_s}(1-\lambda_p)$,where L_b is backwater length, B_c is channel width, λ_p is sediment porosity, Q_s is the sediment supply for a given flow event, and ΔH is the amplitude of bed-elevation adjustments in the backwater zone (estimated by the difference between the high-flow and low-flow normal flow depths; Chatanantavet & Lamb, 2014). The channel-adjustment timescale is based on the simplified scenario where the full sediment supply (Q_s) is deposited within the backwater zone, representing a shortest-possible adjustment time; for the more general case where part of the sediment supply is deposited offshore or on the floodplain, channels should take longer to adjust. Because flow duration T_{flow} was shorter than the adjustment time T_{adj} (Table 1), the backwater zone was kept in a state of perpetual adjustment similar to natural deltaic rivers: riverbed elevation and slope oscillated relative to a mean, convex-upward profile that reflected ongoing competition between low-flow deposition and high-flow erosion (Arkesteijn et al., 2019; Blom et al., 2017). Previous numerical simulations have demonstrated that this condition ($\frac{T_{flow}}{T_{adj}} < 1$) is necessary for backwater-scaled avulsions, and that dynamics are relatively insensitive to the flow duration so long as this condition is upheld (Chadwick et al., 2019). With this in mind, we designed the experiment to satisfy this condition, and relaxed the precise ratio between flow duration and adjustment ($\frac{T_{flow}}{T_{adj}} \sim 0.5$; Table 1) compared to what is usually observed in nature ($\frac{T_{flow}}{T_{adj}} \sim 0.0001 - 0.1$; Chadwick & Lamb, 2021) to ensure the experiment was physically and logistically feasible.

At the upstream end, we covaried sediment supply with water discharge to produce the same normal-flow bed slope ($S = 0.0042$) for high flow and low flow, which was gentle enough to maintain subcritical flow ($Fr < 1$) and a single-thread channel. The flow depth and slope resulted in a backwater length-scale of $L_b = \frac{H_c}{S} = 1.8$ m. It was necessary that L_b be much greater than the channel width (~0.2 m) to observe a significant backwater reach, but also small enough to fit within the laboratory basin (Figure 2a). Water and sediment discharges in CROF18 were similar to CROF16, but were adjusted slightly to improve dynamic scaling with sea-level rise rates.

To isolate the effect of sea-level change on backwater-scaled delta dynamics, we systematically raised and lowered sea level at six different speeds during six distinct phases of the experiment, lettered A–F (Table 2). Rise rate was constant during each phase. Following previous work, we scaled laboratory sea-level rise and fall rates relative to the characteristic rate of aggradation (Chadwick et al., 2020). The dimensionless sea-level rise rate is given by

$$\sigma^* = \frac{\sigma}{H_c/nT_c} \tag{2}$$

where T_c is the channel-filling timescale approximated by $T_c \sim \frac{H_c B_c L_b}{Q_s}(1-\lambda_p)$ (Chatanantavet & Lamb, 2014; Reitz & Jerolmack, 2012), $n = (N+1)/2$ is the number of avulsions before a given deltaic lobe is reoccupied, and N is the average number of delta lobes, for simplicity here taken to be $N = 4$ (Ganti et al., 2019). The denominator of Equation 2 is a first-order estimate of the maximum possible aggradation rate, in the hypothetical limit where all sediment is deposited uniformly across the backwater-scaled topset. Most modern deltas fall in the range $0 < \sigma^* < 1$ (Chadwick et al., 2020). Using estimates of Milankovich-scale sea-level cycles over the Pleistocene and Miocene (~120 m of rise and fall over ~100 ky for Pleistocene, and ~30 m of rise and fall over

$\sim$40 ky for Miocene; Li et al., 2016), we estimate many deltas fall in the range $-1 < \sigma^* < 1$. CROF18 Phases A, B, C, E, and F were selected to fall within this range, and correspond to rise rates of $-3\ \mathrm{mm/hr} < \sigma < 3\ \mathrm{mm/hr}$ (Table 2). Phase D was designed to explore the case where sea level rises faster than the maximum aggradation rate ($\sigma^* > 1$), a possible scenario for many lowland deltas in the next century (Chadwick et al., 2020). While we did not incorporate subsidence into the experiment, delta response to uniform subsidence is expected to be mechanically similar to that of sea-level rise (González & Tornqvist, 2006; Reitz et al., 2015). We allowed each phase to continue long enough to allow for many avulsions. Phases were also kept brief enough that the offshore basin depth did not change by more than a factor of two (Figure 2b); this allowed us to mitigate the effect of changing basin depth on avulsion patterns (Carlson et al., 2018; Wang et al., 2019), and therefore better isolate the effect of sea-level rise rate.

2.2. Data Collection

Overhead images of delta evolution were collected every minute using six mounted cameras that bordered the experimental facility. Photos from each camera were concatenated to ensure a wide field of view that extended beneath railings in the facility. The water was dyed using a fluorescent green dye, allowing for visual distinction between subaerial and submerged surfaces even for shallow ($\sim$1cm) water depths under ultraviolet light fixtures. Before starting a flow event, we inserted $\sim$0.5 gallons of dye into the end tank. We ran the flow using a very low discharge ($Q = 0.002\ \mathrm{L/min}$) with no sediment feed for $\sim$12 hours of standby to allow the dye to disperse evenly through the tank without mobilizing sediment or disturbing the delta.

An ultrasound distance meter (Massa M-5000/220, Massa, Hingham, MA) and laser displacement sensor (Keyence LK-G5000, Keyence Corporation of America, Itasca, IL) measured water surface elevation at 1-mm vertical resolution and bed topography at 0.1-mm resolution. Before each flow event, we adjusted the weir siphon such that sea level followed the curve in Figure 2b; we verified sea level remained in equilibrium with the weir within 0.1 mm by scanning a thin piece of floating wax paper at the downstream end using the laser sensor. At the beginning of each flow event, we collected water surface elevation data, and after each event we switched off the flow and measured bed surface elevation. Topographic scans included a long profile through the river section and basin section along the flume centerline (3-mm horizontal resolution), as well as a series of cross sections in the basin perpendicular to the flume axis (3-mm resolution in the cross-stream direction, spaced every 15 cm in the downstream direction). The basin water level was maintained during bed topography scans, and data for submerged parts of the delta were corrected for the refraction index of the laser beam through still water. The green color of the fluorescent dye in the basin ensured transmission of the red laser signal. Summed errors associated with vertical precision of the instrument and the refraction-index correction were ± 0.1 mm. Raw data from topographic scans were denoised using a median filter of kernel size 1.5 cm.

2.3. Data Analysis

Concatenated overhead images were used to map channel avulsions and shoreline evolution in the experiment. Following previous work, we identified avulsions as the establishment of a new channel (the daughter channel) that captured the majority of flow through consecutive flow events, and the old channel (the parent channel) was partially or completely abandoned (Ganti, Chadwick, Hassenruck-Gudipati, Fuller, & Lamb, 2016). Avulsion location and time were measured as the location and time when the levee breach in the parent channel initiated. Manual identification of avulsions involved a degree of subjectivity; still, our measurements for avulsion location have an uncertainty of less than a channel width and much less than a backwater length-scale, and measurements for avulsion time have an uncertainty of approximately 1 minute (Ganti, Chadwick, Hassenruck-Gudipati, Fuller, & Lamb, 2016; Ganti, Chadwick, Hassenruck-Gudipati, & Lamb, 2016). Avulsion length (L_A) was computed as the distance along the parent channel from the river mouth to the avulsion location. Avulsion frequency was calculated using $f_A = 1/T_A$, where T_A is the time between the current avulsion event and the previous avulsion event. We manually mapped the delta shoreline, following the boundary of fluorescent green water and the brown sediment surface. We also independently mapped the location of the topset-foreset break; during sea-level rise the shoreline sometimes retreated upstream from the topset-foreset break.

We measured channel aggradation and erosion using the time series of topographic scans collected by the laser sensor at the end of each flow event. For cases when topographic scans were collected within 4 min of an avulsion

10.1029/2021JF006422

Table 3
Field Data Used in This Study

	σ [mm/yr]	L_A [km]	L_b [km]	f_A [1/kyr]	Q_s [Mt/yr]	H_c [m]	B_c [km]	B [km]	H_b [m]	N [-]	T_c [kyr]	σ^* [-]	L_A^* [-]	f_A^* [-]	H^* [-]
Parana	3	210	295	0.6	79	11.8	1.3	50.8	40	4	3.6	2.3	0.7	2.2	0.3
Danube	0.2	95	125	0.5	67	6.3	1.3	50	50	4	0.9	0.1	0.8	0.5	0.9
Nile	4.5	210	254	—	120	16.2	0.2	9.6	120	4	0.5	0.4	0.8	—	—
Mississippi	2.3	490	480	0.8	400	21	0.7	26	80	4	1	0.3	1	0.8	0.1
Rhine-Meuse	1.6	51	45.5	0.7	3.1	5	0.7	28	18	4	3.3	2.6	1.1	2.3	—
Magdalena	2.9	67	63.2	—	220	6	1.1	44	200	4	0.1	0.1	1.1	—	—
Orinoco	2.6	78	133.3	1	150	8	2	80	110	4	0.9	0.7	0.6	0.9	0.2
Mid Amazon	2.9	404	400	—	1,200	12	3	120	50	4	0.8	0.5	1	—	—
Rhone	2.8	—	183.5	0.7	31	7.3	0.4	15.1	70	4	1	1	—	0.7	1.4
Yellow	1.7	31	35	142.9	1,100	3.5	0.5	20	30	4	0	0	0.9	0.5	0.1
Goose	−3	—	0.9	3	0.3	2	0.1	4	10	4	0	−0.1	—	0.1	—
Mitchell	−0.3	—	23.3	16	2.9	7	0.1	4	15	4	0.4	0	—	5.7	—
Trinity	4.2	—	31.3	—	6.2	5	0.2	8	8	4	0.3	0.7	—	—	—

Note. Relative sea-level rise rates (σ) are reported by Chadwick et al. (2020) and reflect the sum of eustatic sea-level change (Bintanja et al., 2005) and coastal subsidence (Jelgersma, 1996; Milliman et al., 1989; Syvitski, 2008; Törnqvist et al., 2008; Yu et al., 2012) estimated over the time that avulsions occurred. Avulsions occurred during the late Holocene period (last 7 ky), with the exception of the Huanghe where pre-industrial historical avulsions are documented (Ganti et al., 2014). Avulsion lengths (L_A) and backwater length-scales (L_b) are reported in Chatanantavet et al. (2012) and Ganti et al. (2014). Avulsion frequency (f_A), channel depth (H_c), and channel width (B_c) are reported in Jerolmack & Mohrig (2007). Basin depths (H_b) are reported in Syvitski & Saito (2007). Sediment supplies (Q_s) are reported in Milliman & Syvitski (1992), and are converted here to volumetric rates using a sediment density of 2650 $\mathrm{kg/m^3}$ and 40% porosity $\left(\lambda_p = 0.4\right)$. Channel filling timescales are estimated as $T_c = H_c B_c L_b \left(1 - \lambda_p\right) / Q_s$ following Chatanantavet & Lamb (2014) and Reitz & Jerolmack (2012). Data for the Danube, Goose, Mitchell, and Trinity are compiled from site-specific studies (Giosan et al., 2006; Lane et al., 2017; Moran et al., 2017; Nijhuis et al., 2015). Deltas were assumed to be composed of four lobes ($N = 4$) with width of forty times the channel width ($B = 40 B_c$), which are reasonable estimates (Coleman et al., 1998; Hayden et al., 2019; Pang & Si, 1979; Parker et al., 2008). Avulsion thresholds (H^*) are reported by Chadwick et al. (2020), dimensionless sea-level rise (σ^*) is calculated using Eq. (2), dimensionless avulsion length is calculated as $L_A^* = L_A / L_b$, and dimensionless avulsion frequency is calculated as $f_A^* = f_A T_c$. Empty table entries indicate data were not available.

event, we measured the height of riverbed aggradation at the avulsion node since the previous avulsion, that is, the avulsion threshold (H) (Ganti et al., 2014; Mohrig et al., 2000). When sea-level fall caused valley incision, we calculated the incision depth from the riverbed to the uppermost abandoned fluvial surface.

We did not take stratigraphic cuts of the experiment, but instead constructed synthetic stratigraphy using the time series of topographic scans (Ganti et al., 2011, 2013), which is a good approximation of physical stratigraphy in experimental avulsion-dominated settings (Hajek & Straub, 2017; Straub et al., 2012). Synthetic set boundaries were calculated from topographic scans collected at the end of each flow, and so represent alternating time intervals of 22 min and 8 min. A constant time interval is ideal for constructing synthetic stratigraphy (Paola et al., 2018), but we deemed the alternating intervals were a necessary concession for experimental logistics. Furthermore, we found the alternating time intervals were sufficient to study the effect of floods, avulsions, and sea-level rise on stratigraphy over the experiment: both intervals were relatively short, and the alternation scheme remained constant throughout the entire experiment. Taking cross sections of the synthetic stratigraphy perpendicular to the flume axis on the delta topset, we identified individual depositional beds between erosional surfaces and measured the maximum preserved thickness of each bed (Ganti, Chadwick, Hassenruck-Gudipati, & Lamb, 2016).

2.4. Comparison to Theory and Field Data

We compared experimental results to theoretical predictions and field data for avulsion location (L_A) and frequency (f_A). Field data for avulsions on lowland deltas is reported by Chadwick et al. (2020) (Table 3), compiled from previous work (Bintanja et al., 2005; Chatanantavet et al., 2012; Ganti et al., 2014; Giosan et al., 2006; Jelgersma, 1996; Jerolmack & Mohrig, 2007; Milliman et al., 1989; Syvitski, 2008; Syvitski & Saito, 2007; Törnqvist et al., 2008). For comparison to theory, we focused on the statistical averages of distributions observed in experimental and field data, as well as systematic changes in these distributions. Autogenic variability is expected because avulsions are inherently stochastic in nature and subject to a variety of triggering mechanisms (Hajek & Wolinsky, 2012; Kleinhans et al., 2013). Field data for avulsion frequency are single-value estimates for each delta representing an average over measured Holocene or historic avulsion events (Chadwick et al., 2020; Jerolmack & Mohrig, 2007). Field data for avulsion length are estimated by the modern streamwise distance from the river mouth to the delta apex (Chatanantavet et al., 2012); this approximation is sufficient for our study because delta apices generally originate from a preferential avulsion location, though we note such estimates do not consider how autogenic and allogenic variations can prompt avulsions to occur upstream or downstream of the preferential avulsion length (Chadwick & Lamb, 2021; Chamberlain et al., 2018; Ganti et al., 2014). A comprehensive history of avulsion events and varying basin conditions is available for some of these deltas, including the Rhine-Meuse (cf. Kleinhans, 2010; Stouthamer & Berendsen, 2000) and the Mississippi (cf. Chamberlain et al., 2018; Coleman et al., 1998).

On average, avulsion length has been found to scale with the theoretical length of the backwater zone, which can be approximated by the ratio of the channel depth to downstream slope, $L_b = H_c/S$ (Equation 1; Figure 1c). However, backwater length is more accurately predicted using the Bresse solution, which accounts for how Froude number, flood stage, and shoreline depth can influence the backwater length (Bresse, 1860; Lamb et al., 2012). Under the assumption of steady flow, uniform channel width, and uniform river slope, the Bresse solution is given by

$$L_{b,Bresse} = \frac{H_n}{S}\left[\zeta_u - \zeta_s - \left(1 - Fr^2\right)\left(Z\left(\zeta_u\right) - Z\left(\zeta_s\right)\right)\right] \tag{3}$$

where $L_{b,Bresse}$ is Bresse backwater length, H_n is normal flow depth, and $\zeta = H/H_n$ is the ratio of the flow depth H to the normal-flow depth evaluated at the shoreline (ζ_s) and at the upstream end of the backwater zone (ζ_u). Following Lamb et al. (2012), we used H_n and Fr during low-flow conditions ($H_n = 7.5$ mm; $Fr = 0.43$), estimated ζ_s using the high-flow depth as a proxy for shoreline depth ($\zeta_s = \frac{11.7\text{ mm}}{7.5\text{ mm}} = 1.56$), and identified the upstream end of the backwater zone based on a <5% deviation from the normal-flow depth ($\zeta_u = 0.95$). The $Z(\zeta)$ operator is defined by

$$Z(\zeta) = \frac{1}{6}\ln\left(\frac{\zeta^2 + \zeta + 1}{(\zeta - 1)^2}\right) - \frac{1}{\sqrt{3}}\arctan\left(\frac{\sqrt{3}}{2\zeta + 1}\right) \tag{4}$$

The Bresse solution also provides estimates of the length of water-surface drawdown and scour during high flows. We estimated scour length $L_{d,Bresse}$ using Equation 4 by conversely taking H_n and Fr during high flow conditions ($H_n = 11.7$ mm; $Fr = 0.59$) and using low-flow depth as a proxy for shoreline depth ($\zeta_s = \frac{7.5\text{ mm}}{11.7\text{ mm}} = 0.64$) (Lamb et al., 2012). It has been hypothesized that avulsion lengths fall within the range $L_{d,Bresse} < L_A < L_{b,Bresse}$, corresponding to avulsion sites within the backwater zone and upstream of prominent scour during drawdown (Brooke et al., 2020; Ganti et al., 2019). Equations 5 and 6 yield predicted values of $L_{d,Bresse} = 0.9$ m and $L_{b,Bresse} = 1.8$ m for the CROF18 experiment.

Avulsions tend to occur through gradual channel aggradation that renders flow in the initial channel gravitationally unstable—termed the setup period—followed by the triggering period that reroutes flow to the new channel (Kleinhans et al., 2013; Slingerland & Smith, 2004). The triggering period can depend on site-specific conditions involving bifurcations (Salter et al., 2018); overbank flooding (Edmonds et al., 2009); crevasse-splay deposition and erosion (Slingerland & Smith, 1998); and channel migration and headward erosion of secondary channels (Aslan et al., 2005). In contrast, the setup period is similar across settings: it is achieved through gradual channel aggradation. We focus our experimental and theoretical analysis on the setup period, which is important for determining when and where avulsions take place (Hajek & Wolinsky, 2012). In particular, the frequency of avulsion f_A has been found to scale inversely with the time required for the riverbed to aggrade to a height of the channel depth,

$$f_A \propto \frac{1}{T_c} = \frac{v_a}{H_c} \tag{5}$$

where T_c is the channel-filling timescale, here defined as the ratio of the channel depth H_c and aggradation rate v_a ($T_c \equiv H_c/v_a$) (Jerolmack & Mohrig, 2007; Reitz & Jerolmack, 2012). Over timescales of T_c, the river aggrades to a critical height comparable to the channel depth, rendering it gravitationally unstable and ready to transition to the triggering period wherein avulsion occurs (Mohrig et al., 2000). The triggering period is not instantaneous (Kleinhans et al., 2013), but for simplicity Equation 5 considers the duration of the triggering period to be negligible compared to the duration of the setup period (Hajek & Wolinsky, 2012).

Predicting avulsion frequency using Equation 5 requires the knowledge of the average aggradation rate v_a during the setup period, which depends on sea-level rise, sediment supply, backwater effects, and progradation into the offshore basin (Jerolmack, 2009; Reitz & Jerolmack, 2012). Chadwick et al. (2020) developed an analytical model for v_a that accounts for these processes by partitioning sediment between topset and foreset. Under the simplifying assumptions that avulsion length (L_A) is known a priori and topset slope (S) is constant and much gentler than the foreset slope, the model result is

$$f_A = \begin{cases} \dfrac{1}{1-\lambda_p}\dfrac{Q_s}{(L_A - D)\,BH + DB\,(H_b + z + DS/2)} & \text{if } D \geq 0 \\ \dfrac{1}{1-\lambda_p}\dfrac{Q_s}{L_A BH} & \text{if } D < 0 \end{cases} \tag{6}$$

where $D = \frac{H-z}{S}$ is lobe-progradation distance, $z = n\sigma f_A^{-1}$ is the cumulative height of sea-level rise during an inter-avulsion period, and H_b is the basin depth (Figure 2). The term B is the width of deposition, which in the absence of floodplain deposition is here approximated using the channel width (20 cm). The height of aggradation between avulsions, H, and the avulsion length, L_A, were measured during the experiment. For $D \geq 0$, the first and second terms in the denominator describe sediment partitioned to the delta-lobe topset and foreset, respectively. For $D < 0$, all sediment is partitioned to the topset.

2.5. Dimensionless Variables

Experimental and field data were placed in a nondimensional framework. First, the dimensionless avulsion length, L_A^*, was calculated as the ratio of the avulsion length to the backwater length-scale ($L_A^* = L_A/L_b$) (Ganti, Chadwick, Hassenruck-Gudipati, Fuller, & Lamb, 2016), which is approximately equal to one for a backwater-scaled delta (Equation 1; Figure 1c). Second, the dimensionless avulsion frequency, f_A^*, was defined as the ratio of the avulsion frequency to the inverse of the channel-filling timescale ($f_A^* = \frac{f_A}{1/T_c}$; Equation 5), where the channel-filling timescale was approximated by $T_c \sim \frac{H_c B_c L_b}{Q_s}(1-\lambda_p)$ (Chatanantavet & Lamb, 2014; Reitz & Jerolmack, 2012). Avulsion frequency scales inversely with the channel-filling timescale, so f_A^* is typically of order unity (Chadwick et al., 2020; Ganti et al., 2014; Reitz & Jerolmack, 2012). Dimensionless sea-level rise rate, σ^*, was calculated using Equation 2. Lastly, we calculated the dimensionless avulsion threshold, H^* (Ganti et al., 2014), defined as the ratio between the height of aggradation between avulsions and the channel depth ($H^* = H/H_c$).

3. Results

3.1. Observations From Phases A–F

During experimental Phase A, a backwater-scaled delta formed under constant sea-level conditions ($\sigma^* = 0$) similar to previous experiments (Ganti, Chadwick, Hassenruck-Gudipati, Fuller, & Lamb, 2016; Ganti, Chadwick, Hassenruck-Gudipati, & Lamb, 2016) (Movie S1). After an initial period of sheet-flow (0–18 hr), flow channelized and the delta grew through repeated avulsions during run time 18–43.3 hr. An example avulsion cycle is presented in Figures 3a and 3b for run time 33–38 hr. The river initially flowed northeastward (Figure 3a), and over the course of 5 hr gradually migrated eastward before avulsing at 38 hr (Figure 3b). Foreset deposition occurred at the river mouth, resulting in localized progradation along the northern and eastern shoreline. The avulsion occurred within the backwater zone, at a site 1.5 m upstream of the river mouth ($L_A = 1.5$ m) where channel aggradation was maximized (Figures 3c–3e), consistent with earlier backwater-scaled experiments (Ganti, Chadwick, Hassenruck-Gudipati, Fuller, & Lamb, 2016; Ganti, Chadwick, Hassenruck-Gudipati, & Lamb, 2016) and numerical models (Chadwick et al., 2019; Chatanantavet et al., 2012). Immediately before the avulsion, the riverbed reached an aggradation height of ~5 mm at the avulsion site, approximately two-thirds the average channel depth (7.5 mm) (Figure 3d). Low and high flows contributed to channel aggradation at the

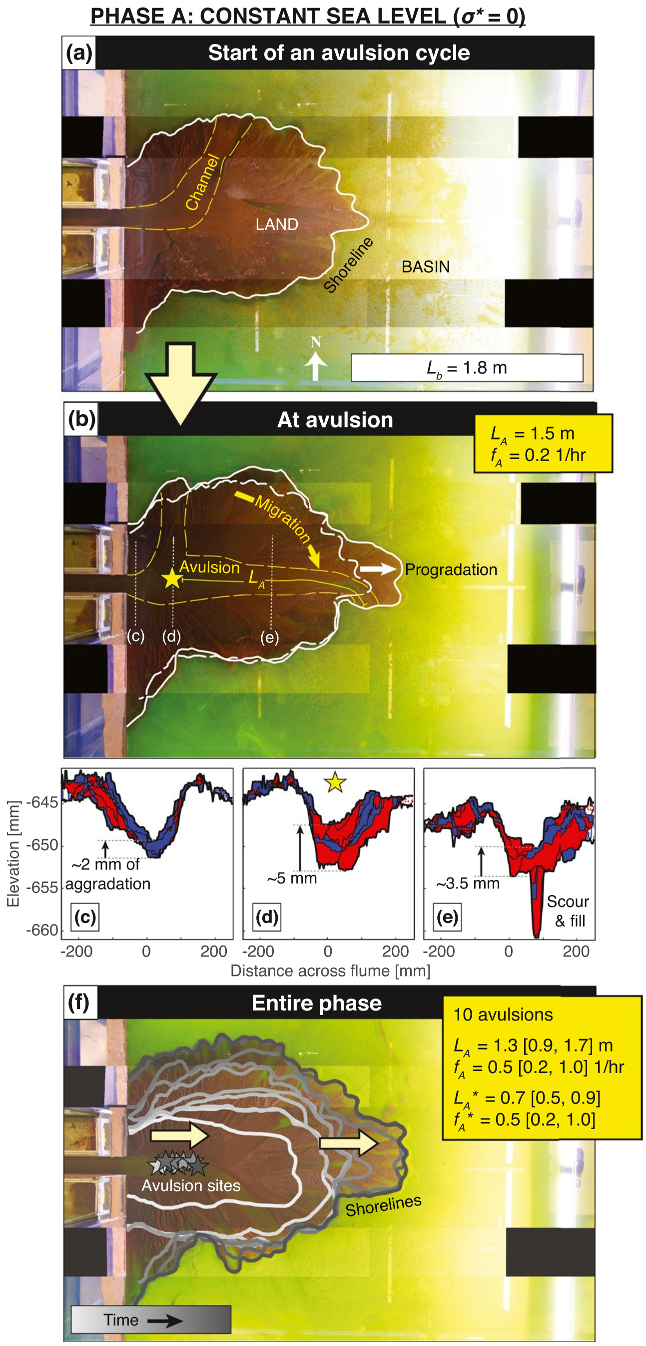

Figure 3. Experimental results for constant sea-level conditions (CROF18 Phase A). (a) Overhead image taken at the beginning of an avulsion cycle, highlighting the main channel (yellow dashed lines) and shoreline (white line). (b) Image of the delta during an avulsion, where the flow was diverted to a new channel at the avulsion site (yellow star). Avulsion length L_A was measured as the distance between the shoreline and the avulsion site along the parent channel centerline (solid yellow line). Yellow arrow highlights gradual channel migration, and white arrow indicates shoreline progradation since panel (a). (c–e) Cross sections of channel aggradation along profiles labeled in (b). Channel aggradation associated with low flows and high flows is color-coded blue and red, respectively. Yellow star indicates profile at the avulsion site. (f) Overhead image showing the time series of avulsion sites (stars) and shorelines (lines) during Phase A, color-coded from light to dark with increasing time. Arrows highlight long-term movement of the shoreline and avulsion node.

avulsion site (see blue-shaded and red-shaded deposits in Figure 3d). Upstream of the avulsion site, aggradation was reduced (~2 mm) and primarily occurred during low flows (Figure 3c). Downstream of the avulsion site, aggradation was similarly reduced (~3.5 mm) and was associated with predominantly high-flow deposits that filled deep scours (Figure 3e). Bed scours were ~50 cm in length. Scours were associated with water-surface

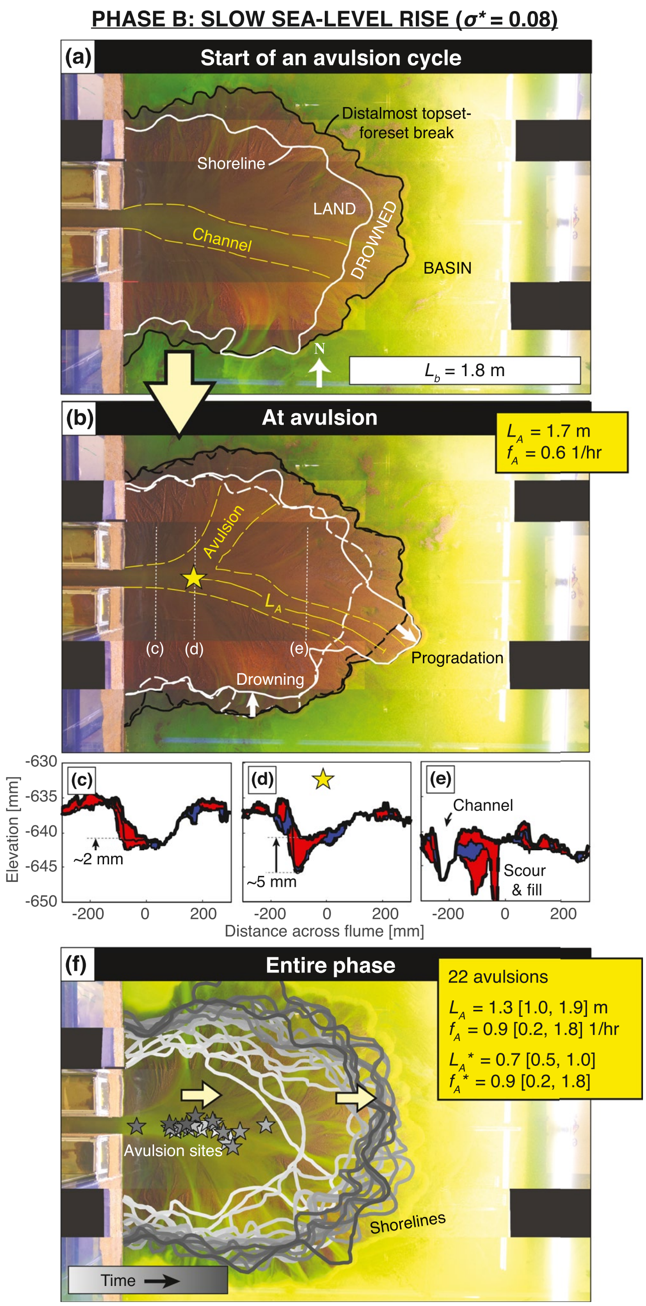

Figure 4. Experimental results for slow sea-level rise conditions (CROF18 Phase B). (a) Overhead image taken at the beginning of an avulsion cycle, highlighting the main channel (yellow dashed lines), shoreline (white line), and distalmost topset-foreset break (black line). (b) Image of the delta during an avulsion, where the flow was diverted to a new channel at the avulsion site (yellow star). Avulsion length L_A was measured as the distance between the shoreline and the avulsion site along the parent channel centerline (solid yellow line) (c–e) Cross sections of channel aggradation along profiles labeled in (b). Channel aggradation associated with low flows and high flows is color-coded blue and red, respectively. Yellow star indicates profile at the avulsion site. (f) Overhead image showing the time series of avulsion sites (stars) and shorelines (lines) during Phase B, color-coded from light to dark over time. Arrows highlight long-term movement of the shoreline and avulsion node.

drawdown during high flows (Ganti et al., 2019; Trower et al., 2018), and were filled in during subsequent flows. In the absence of sea-level rise and subsidence, aggradation was primarily caused by shoreline progradation.

Results were similar for the rest of Phase A. A total of 10 avulsions occurred (Figure 3f), with an average frequency of $f_A = 0.5\,\mathrm{hr}^{-1}$ and ranging from $0.2\,\mathrm{hr}^{-1}$ to $1.0\,\mathrm{hr}^{-1}$, hereafter abbreviated as $f_A = 0.5\,[0.2,\ 1.0]\,\mathrm{hr}^{-1}$. Avulsions were abrupt, usually initiating at the start of a high flow event and completing within 1 min. Each avulsion was associated with localized progradation near the active river mouth. Avulsions occurred between 0.3 and 0.5 m downstream of the basin inlet. Avulsion locations moved downstream on average in tandem with shoreline progradation, as expected (Ganti, Chadwick, Hassenruck-Gudipati, & Lamb, 2016; Ganti et al., 2014; Moodie et al., 2019). Avulsion length was 1.3 m on average, with a minimum of 0.9 m and a maximum of 1.7 m ($L_A = 1.3\,[0.9,\ 1.7]$ m). All avulsion lengths were less than the backwater length (1.8 m) and greater than or equal to the drawdown length (0.9 m) calculated using the Bresse approximation, consistent with previous work (Ganti et al., 2019; Lamb et al., 2012). Nondimensionalization yields $L_A^* = 0.7\,[0.5,\ 0.9]$ and $f_A^* = 0.5\,[0.2,\ 1.0]$ (Table S1; Figure S1 in Supporting Information S1).

Phase B featured slow sea-level rise (0.25 mm/hr; $\sigma^* = 0.08$) from 43.3 to 82 hr, resulting in more frequent avulsions and transient land loss between avulsions. An exemplary avulsion cycle is shown for 59.4–61 hr (Figures 4a and 4b). The river flowed from west to east, and sea-level rise caused drowning of the delta topset such that the shoreline was decoupled from the topset-foreset break (Figure 4a). River mouth deposition caused shoreline progradation that locally counteracted land loss, reuniting the shoreline and topset-foreset break along the eastern shoreline (Figure 4b). The northern shoreline remained relatively stable and the southern shoreline experienced further land loss. Similar to Phase A, the avulsion occurred where and when the channel had aggraded by ~5 mm, approximately two-thirds the channel depth (Figures 4c–4e). However, compared to Phase A the avulsion occurred more rapidly ($f_A = 0.6\,\mathrm{hr}^{-1}$) because sea-level rise caused higher aggradation rates (Bryant et al., 1995; Martin et al., 2009). Aggradation was consistently reduced upstream of the avulsion site (Figure 4c), as well as downstream of the avulsion site where scour-and-fill features indicate intermittent erosion during high flows (Figure 4e), similar to Phase A (Figures 3c–3e).

Results were similar for the rest of Phase B, during which we observed 22 avulsions. Sea-level rise caused avulsions to occur ~50% more frequently than during constant sea-level conditions, at a pace of $f_A = 0.9\,[0.2,\ 1.8]\,\mathrm{hr}^{-1}$ (Figure 4f), corresponding to dimensionless avulsion frequency $f_A^* = 0.9\,[0.2,\ 1.8]$. Avulsion length was relatively unchanged ($L_A = 1.3\,[1.0,\ 1.9]$, $L_A^* = 0.7\,[0.5,\ 1.0]$), indicating that avulsions continued to occur in the upstream half of the backwater zone during sea-level rise. Each avulsion featured localized progradation near the river mouth and shoreline retreat along sediment-starved coastlines due to sea-level rise. Progradation outpaced retreat on average, leading to net growth of the land area during Phase B (Figure 4f), albeit at a slower pace than during Phase A (Figure 3f) (Table S1; Figure S1 in Supporting Information S1).

During Phase C (82–101 hr), sea-level rise was increased fourfold to 1 mm/hr ($\sigma^* = 0.33$), resulting in even more frequent avulsions and a gradual landward shift of the shoreline and avulsion node. An exemplary avulsion cycle

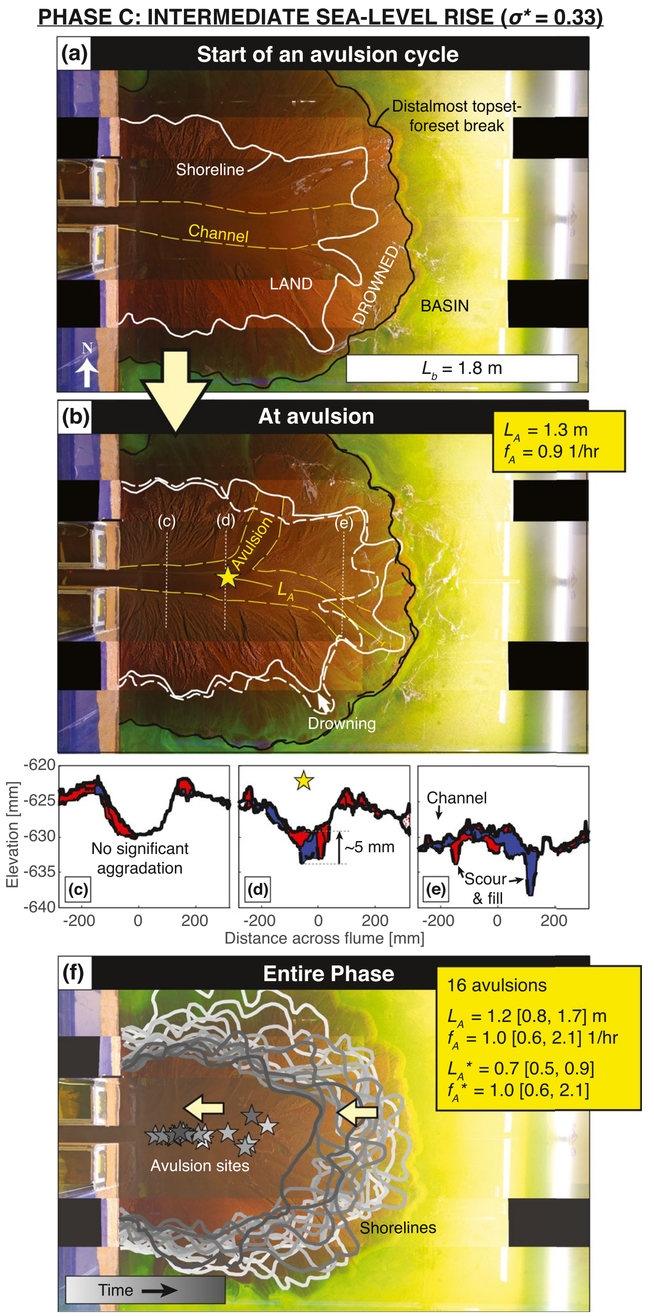

Figure 5. Experimental results for intermediate sea-level rise conditions (CROF18 Phase C). (a) Overhead image taken at the beginning of an avulsion cycle, highlighting the main channel (yellow dashed lines), shoreline (white line), and distalmost topset-foreset break (black line). (b) Image of the delta during an avulsion, where the flow was diverted to a new channel at the avulsion site (yellow star). Avulsion length L_A was measured as the distance between the shoreline and the avulsion site along the parent channel centerline (solid yellow line) (c–e) Cross sections of channel aggradation along profiles labeled in (b). Channel aggradation associated with low flows and high flows is color-coded blue and red, respectively. Yellow star indicates profile at the avulsion site. (f) Overhead image showing the time series of avulsion sites (stars) and shorelines (lines) during Phase C, color-coded from light to dark over time. Arrows highlight long-term movement of the shoreline and avulsion node.

is presented in Figures 5a and 5b. Sediment deposition at the river mouth caused localized shoreline progradation, similar to Phases A–B. Unlike earlier phases, this progradation was insufficient to fully counteract land loss (Figure 5b); the shoreline did not reach the distal-most topset-foreset break when avulsion occurred, and sea-level rise caused more extensive shoreline retreat in sediment-starved areas. At the time of the avulsion, the channel bed aggraded by ∼5 mm at the avulsion site (Figure 5d), with reduced aggradation both upstream (Figure 5c) and downstream (Figure 5e), similar to earlier phases. However, accelerated aggradation due to sea-level rise allowed the avulsion to occur more quickly ($f_A = 0.9$) than earlier phases.

We observed similar behavior for the other 15 avulsions of Phase C. Accelerated sea-level rise caused avulsions to occur at a frequency of $f_A = 1.0\,[0.6, 2.1]\,\mathrm{hr}^{-1}$ ($f_A^* = 1.0\,[0.6, 2.1]$) (Figure 5f), on average 10% faster than during slow sea-level rise of Phase B and 60% faster than during constant sea-level conditions of Phase A. The shoreline shifted landward on average (Figure 5f), and the avulsion node gradually migrated landward and maintained a constant avulsion length to the river mouth, consistent with model predictions (Chadwick et al., 2020; Ratliff et al., 2021). Avulsion length scaled with backwater length and was statistically similar to earlier phases ($L_A = 1.2\,[0.8, 1.7]$; $L_A^* = 0.7\,[0.5, 0.9]$) (Figure 5f; Table S1; Figure S1 in Supporting Information S1).

Phase D (101–105 hr) featured another fourfold increase in sea-level rise rate ($4\,\mathrm{mm/hr}; \sigma^* = 1.33$), which caused the channel to avulse rapidly until the delta topset drowned. The first avulsion occurred after only 24 min ($f_A = 2.5\,\mathrm{hr}^{-1}$) (Figures 6a and 6b), followed by a second avulsion 35 min later ($f_A = 1.6\,\mathrm{hr}^{-1}$) (Figure 6c). Averaging these two events yields an avulsion frequency of $f_A = 2.0$ $\left(f_A^* = 2.0\right)$, approximately double the frequency during the previous phase (Figure 4f) and four times that during constant sea-level conditions (Figure 3f). Limited temporal resolution of our scan data prohibits accurate quantification of channel aggradation between avulsions, but avulsion length was comparable to earlier phases ($L_A = 1.1\,\mathrm{m}, 0.8\,\mathrm{m}; L_A^* = 0.6, 0.4$), suggesting aggradation patterns were similar. Unlike previous phases, however, there was no localized shoreline progradation at the river mouth (Figures 6b and 6c). Instead, the active river mouth retreated because nearly the entire sediment load was deposited farther upstream, consistent with numerical predictions under $\sigma^* > 1$ conditions (Chadwick et al., 2020). The limited sediment that reached the river mouth was deposited in a series of upstream-dipping mouth-bar deposits (Figure 6e). The shoreline retreated with each avulsion cycle, and by 102 hr the delta was completely submerged save for intermittent levee deposits at the river mouth (Figure 6d). From this point onward, sediment deposition was primarily restricted to the confined river section where avulsions were not possible (Table S1; Figure S1 in Supporting Information S1).

During Phase E (105–140 hr), sea level dropped at a rate of $0.1\,\mathrm{mm/hr}$ ($\sigma^* = -0.03$), allowing for the resumption of shoreline progradation and avulsions. An example avulsion cycle during 112–113.5 hr is provided in Figures 7a and 7b. The river initially flowed northeastward (Figure 7a), and over the course of 1.5 hr migrated eastward before avulsing at a site 1.1 m upstream of the river mouth (Figure 7b). River-mouth deposition caused localized shoreline progradation, with relatively stable shorelines elsewhere, similar to behavior observed during constant sea-level conditions. Despite sea-level fall, the channel continued to aggrade and avulse due to shoreline

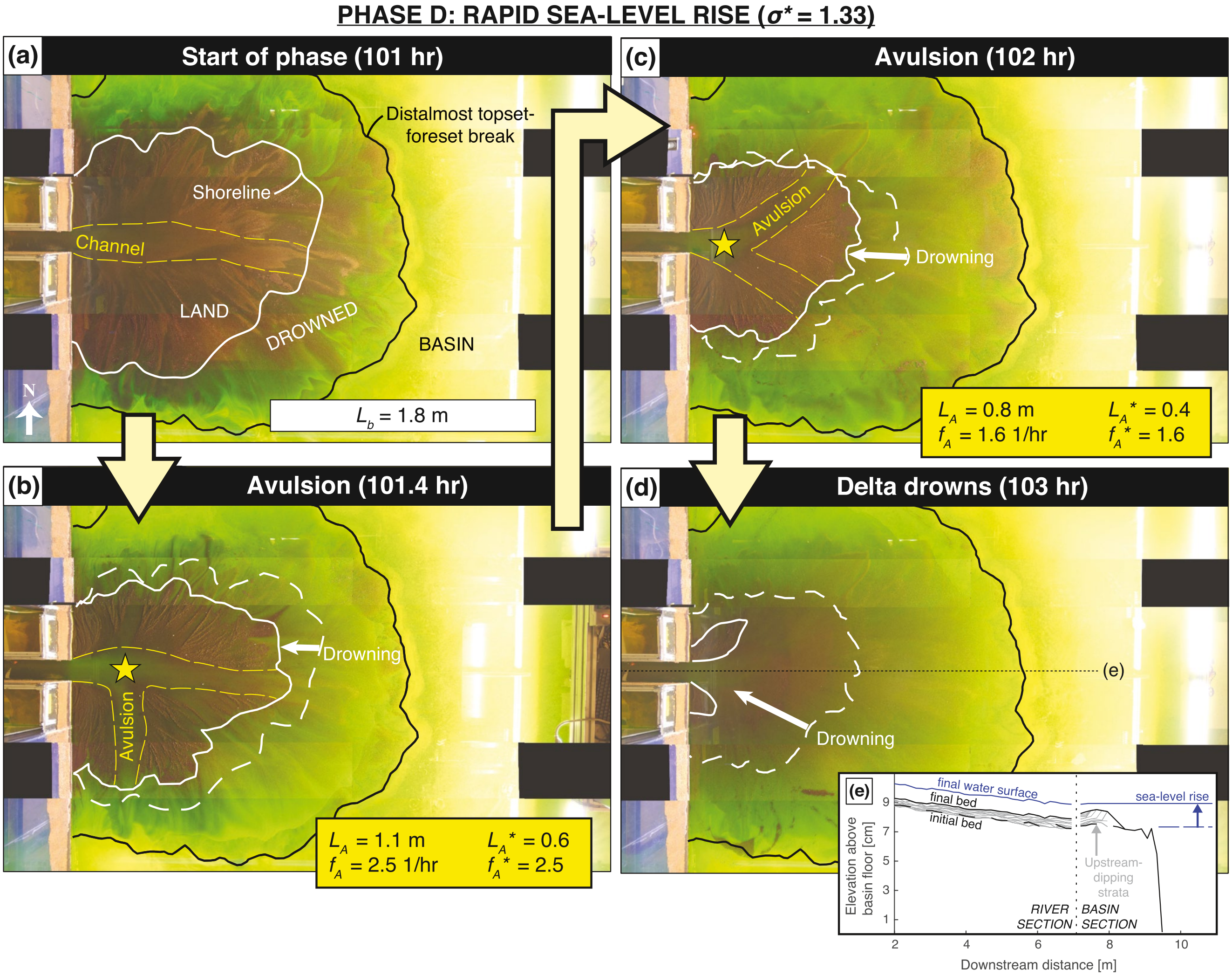

Figure 6. Experimental results for rapid sea-level rise conditions (CROF18 Phase D). (a) Overhead image taken at the beginning of Phase D, highlighting the main channel (yellow dashed lines), shoreline (white line), and distalmost topset-foreset break (black line). (b) Image of the delta during the first avulsion, where the flow was diverted to a new channel at the avulsion site (yellow star). (c) Image of the delta during the second avulsion. (d) Image of the delta at the time when it was fully submerged by sea-level rise. (e) Long-profile evolution of the main channel along profile indicated in panel (d). Bed topography (black) is shown for the start (dashed line) and end (solid line) of Phase D, with synthetic stratigraphy shown in gray. Solid blue line shows final water surface and dashed vertical line indicates the boundary between the flume river section and basin section.

progradation (Figures 7c–7e), consistent with previous work (Bijkerk et al., 2016; Lane et al., 2017; Nijhuis et al., 2015). The avulsion occurred when and where aggradation first reached a height of ∼5mm (Figures 7c–7e) similar to earlier phases (Figures 3d, 4d and 5d). Scour-and-fill deposits were deeper (Figure 7e) and extended farther upstream than in earlier phases, sometimes as far upstream as the avulsion site (Figure 7d). These autogenic scours may have been enhanced by sea-level fall that contributed to water-surface drawdown during high flows (Trower et al., 2018).

Results were similar for the remainder of Phase E, during which we observed 22 avulsions. Avulsion length was statistically similar to earlier phases ($L_A = 1.4\,[1.1,\ 1.8]$ m; $L_A^* = 0.8\,[0.6,\ 1.0]$), with avulsions occurring at a persistent spatial node that migrated downstream with shoreline progradation (Figure 7f). Avulsions occurred at a rate of $f_A = 0.8\,[0.2,\ 1.1]$ ($f_A^* = 0.8\,[0.2,\ 1.1]$), more quickly than during constant sea-level conditions (Figure 3f). Avulsions were frequent because water depths were shallow over the drowned topset from Phases C and D (∼1.5 cm), compared to deeper waters over the basin floor where earlier progradation occurred (∼8 cm) (Figure 7d). Shallow water depths allowed the river mouth to prograde rapidly, which in turn caused the channel to aggrade and avulse more quickly (Carlson et al., 2018; Wang et al., 2019). As a result, we observed ∼1.4 cm of

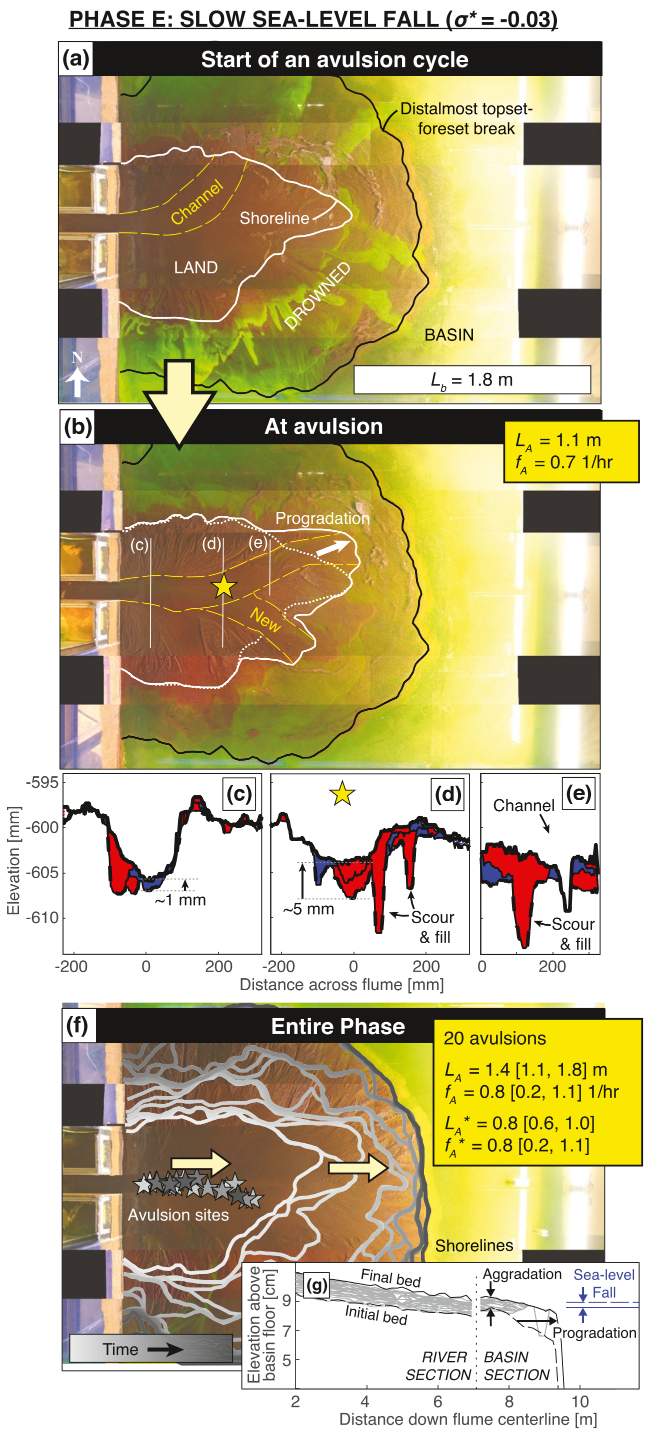

Figure 7. Experimental results for slow sea-level fall conditions (CROF18 Phase E). (a) Overhead image taken at the beginning of an avulsion cycle, highlighting the main channel (yellow dashed lines), shoreline (white line), and distalmost topset-foreset break (black line). (b) Image of the delta during an avulsion, where the flow was diverted to a new channel at the avulsion site (yellow star). (c–e) Cross sections of channel aggradation along profiles labeled in (b). Channel aggradation associated with low flows and high flows is color-coded blue and red, respectively. Yellow star indicates profile at the avulsion site. (f) Overhead image showing the time series of avulsion sites (stars) and shorelines (lines) during Phase E, color-coded from light to dark over time. Arrows highlight long-term movement of the shoreline and avulsion node. (e) Long-profile evolution of the main channel. Bed topography (black) is shown for the start (dashed line) and end (solid line) of Phase E, with synthetic stratigraphy shown in gray. Dashed vertical line indicates the boundary between the flume river section and basin section.

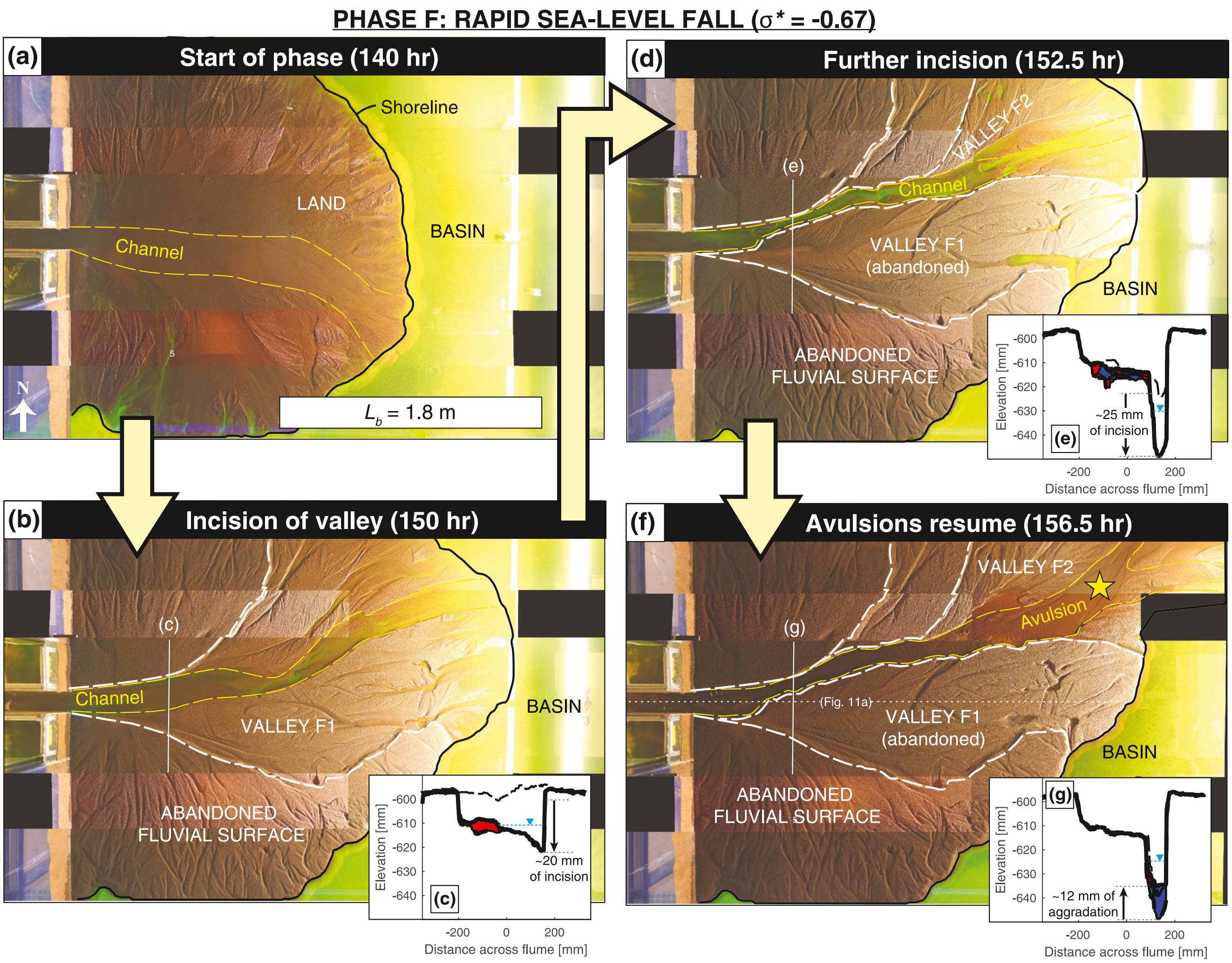

Figure 8. Experimental results for rapid sea-level fall conditions (CROF18 Phase F). (a) Overhead image taken at the beginning of Phase F, highlighting the main channel (yellow dashed lines), shoreline, and distalmost topset-foreset break (black line). (b) Image of the delta during incision of the first valley, Valley F1. White dashed lines are valley walls. (c) Cross section showing valley incision along profile marked in panel (b), including the initial surface (dashed black line) and final surface (solid black line). (d–e) Image and cross section of the delta during incision of the second valley, Valley F2. (f–g) Image and cross section of the delta after aggradation and avulsions resumed. Yellow star indicates avulsion.

aggradation and 20 avulsions throughout Phase E, despite 0.35 cm of sea-level fall (Figures 7f and 7g; Table S1; Figure S2 in Supporting Information S1).

Phase F (140–163.5 hr) featured rapid sea-level fall (2 mm/hr), which caused an initial period of channel incision followed by the resumption of channel aggradation and avulsion. During the first 10 hours, channel incision formed a valley, referred to as Valley F1, and the fluvial surface to the north and south of the valley was abandoned (Figures 8a and 8b). By 150 hr, Valley F1 was incised by ~20 mm, more than 2.5 times the channel depth (Figure 8c). Valley F1 was as narrow as the channel at the flume inlet and widened to more than 10 channel widths (~2m) at the shoreline because gradual channel migration eroded the valley walls (Figure 8b). Channel migration was also associated with lateral accretion, causing intermittent deposition along channel banks within Valley F1 (Figure 8c).

At 150 hr, the channel abandoned most of the Valley F1 surface and incised a new nested valley, Valley F2 (Figures 8d and 8e). Valley F2 formed because the river was unable to erode the full extent of Valley F1 at pace with sea-level fall. Areas near the walls of Valley F1 were less frequented by the migrating channel. As a result, these areas eroded more slowly, and were eventually abandoned when differential erosion left them perched above the channel. The channel was entrenched; increased sediment yield from taller banks hindered lateral

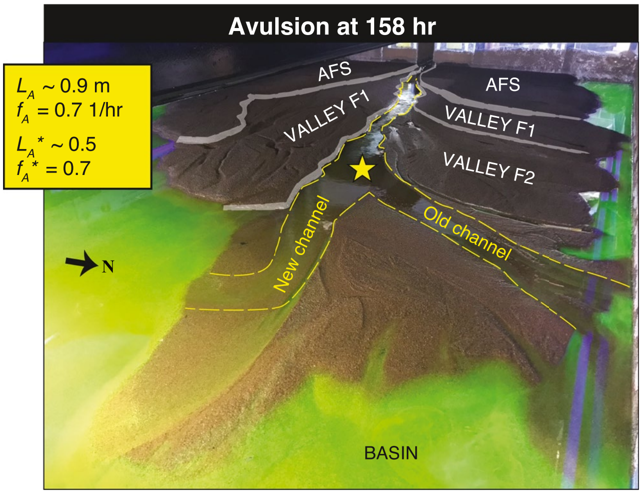

Figure 9. Oblique view of an avulsion during rapid sea-level fall of Phase F. Star is avulsion location, yellow dashed lines are banks of old and new channel, and gray shading highlights valley walls dividing Valley F2, Valley F1, and the abandoned fluvial surface.

migration, and forced the channel to progressively narrow by a factor of three (from ∼150 mm to ∼50 mm) and deepen by a factor of two (from ∼9 mm to ∼18 mm) (Figures 8c–8e). The deepened channel entrained more sediment from the riverbed, resulting in a pulse of incision and further entrenchment. This positive feedback between entrenchment and incision has been documented in earlier fan-delta experiments subjected to steady sea-level fall (Muto & Steel, 2004), as well as alluvial fans in subsiding basins (Malatesta et al., 2017; Pelletier & DeLong, 2004) and bedrock terraces in uplands (Limaye & Lamb, 2016). Over the next 2.5 hr, Valley F2 incised ∼25 mm, rendering the channel entrenched by more than three channel depths relative to Valley F1 and six channel depths relative to the initial fluvial surface (Figure 8e). Valley F2 was narrowest in the upstream ∼2 m of the basin, and gradually widened basinward to nearly seven times the width of the channel (∼1.4 m). Near the shoreline, the channel was free to migrate and rework sediment on the valley floor similar to Valley F1.

At 152.5 hr, the channel resumed aggradation within Valley F2 and 4 hours later the first avulsion occurred (Figure 8f). Aggradation and avulsion occurred despite constant sea-level fall because progradation counteracted incision as the offshore basin shallowed. By 156.5 hr, cumulative sea-level fall had caused the basin depth to shallow to nearly half its depth at the start of Phase F (from 8.6 to 5.2 cm). River-mouth progradation accelerated as the basin shallowed (cf., Bijkerk et al., 2016; Carlson et al., 2018) and by 152.5 hr progradation reached a pace sufficient to cause aggradation during sea-level fall. The channel aggraded by ∼12 mm near the flume inlet (Figure 8g), although we expect aggradation was reduced downstream at the avulsion site because the channel was wider and unconfined by valley walls. Two more avulsions occurred during Phase F, at 158 and 160.45 hr, yielding an average avulsion frequency that was comparable to that during constant sea-level conditions ($f_A = 0.5\,[0.4, 0.7]$). Avulsion length data is limited because overhead photos did not extend to the distal-most river mouth, but handheld cameras captured oblique photos that show avulsion lengths were comparable to earlier phases ($L_A \sim 0.9$ m) (Figure 9). Avulsion length scaled with the backwater length ($L_A \sim 0.5\,L_b$) and avulsions occurred on the unconfined plain of Valley F2 (Figure 9), demonstrating that the avulsion node originated from backwater effects similar to earlier phases, rather than changes in valley confinement (Chadwick et al., 2019; Ganti et al., 2014). The experiment was concluded at 163.5 hr when the river mouth had prograded to the downstream end of the ocean basin (Table S1; Figure S1 in Supporting Information S1).

3.2. Testing Models of Avulsion Location and Avulsion Frequency

We tested avulsion models in terms of the ratio of the avulsion length to the backwater length-scale ($L_A^* = L_A/L_b$) and the ratio of the avulsion frequency to the inverse of the channel-filling timescale ($f_A^* = \frac{f_A}{1/T_c}$; Equation 5) using a nondimensional framework (see Section 2.5). The distribution of avulsion lengths from CROF18 is approximately constant and scales with the backwater length during sea-level rise despite major changes in shoreline position. Avulsion lengths reflect a preferential avulsion node within the backwater zone ($L_A \leq L_{b,Bresse} = 1.8$ m) that is upstream of the zone of prominent scour during high flows ($L_A \geq L_{d,Bresse} = 0.9$ m), consistent with theory (Bresse, 1860; Brooke et al., 2020; Lamb et al., 2012). Dimensionless avulsion length values cluster in the range of $0.5 < L_A^* < 1$ similar to field data and the CROF16 experiment (Figure 10a). Avulsion length does not vary significantly with rise rate, suggesting that while sea-level rise affects the rate of channel aggradation, it does not control where aggradation rate is maximized (Figures 3c–3e, Figures 5c–5e, Figures 6c–6e). The avulsion location, to first order, moves landward or seaward in tandem with the shoreline.

Results show avulsions are more frequent during sea-level rise (phases B and C) compared to steady sea-level conditions (Phase A; Figure 10b). This trend is consistent with field data, the earlier CROF16 experiment, and the analytical model of Equation 6 within uncertainty (Equation 6; Text S1 in Supporting Information S1). Within the regime $0.1 < \sigma^* < 1$, referred to as the rise-dominated regime, sea-level rise rate is comparable to but less than the maximum possible aggradation rate (Equation 2). Increasing rise rate within this regime causes the delta to partition a greater fraction of its sediment supply to channel aggradation on the delta topset, at the expense of

10.1029/2021JF006422

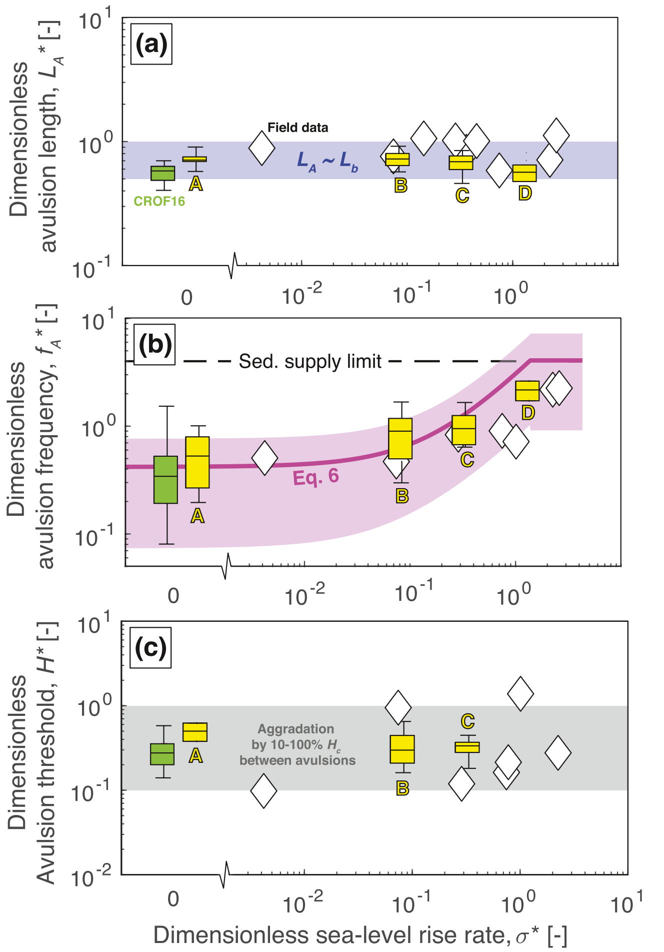

Figure 10. Results for dimensionless (a) avulsion length, (b) avulsion frequency, and (c) avulsion threshold as a function of dimensionless sea-level rise rate (Equation 2). Yellow box plots are CROF18 results for Phases A–D, green box plots are CROF16 results (Ganti et al., 2016b), and yellow diamonds are field data (Table 3). Blue shaded region in (a) is prediction for backwater-scaled avulsions (Equation 1). Magenta line and shaded region in (b) are model prediction from Equation 6 with propagated ±1 standard deviation uncertainty from variability of input parameters L_A, H, and H_b, and black dashed line shows upper limit of avulsion frequency where all sediment is deposited on the lobe topset (Equation 6 for $D < 0$). Shaded region in (c) is expected range of avulsion threshold corresponding to aggradation of the channel by 10%–100% of the channel depth between avulsions (Ganti et al., 2014; Mohrig et al., 2000). Limited temporal resolution of scan data prohibits measurement of avulsion threshold for Phase D. Simplified visualization without shaded regions is provided in Figure S3 in Supporting Information S1.

foreset progradation, allowing for more frequent avulsions. This behavior is documented in CROF18, where we observed an increase in channel aggradation rate (Figures 3, 4 and 5d) and a decrease in progradation rate (Figures 3f, 4f and 5f) as sea-level rise accelerated.

At lower dimensionless rise rates ($\sigma^* < 0.1$; Phase A), experimental results show avulsion frequency is insensitive to sea-level rise rate (Figure 10b). Under these conditions, sea-level rise is slow compared to the pace of delta aggradation (Equation 2), and channel aggradation rate is primarily controlled by the rate of river mouth progradation. In this progradation-dominated regime, avulsion frequency is especially sensitive to offshore basin depth, which sets the rate that the sediment supply can prograde the shoreline. For example, in CROF18, avulsions were more frequent during Phase E (Figure 7) than during Phase A (Figure 3) because the shoreline prograded more quickly across shallow waters overlying the drowned delta top (Figure 7). Furthermore, avulsion frequency was reduced during CROF16 compared to CROF18 Phase A (Figure 10b) because CROF16 featured a deeper offshore basin (10 cm) compared to CROF18 Phase A (4.5 cm; Figure 2).

At higher dimensionless rise rates ($\sigma^* > 1$), corresponding to Phase D, the dimensionless avulsion frequency reaches a maximum value (Figure 10b). This condition is termed the supply-limited regime and corresponds to sea level rising faster than the maximum possible rate the delta can aggrade with the input sediment supply (Equation 2) (Chadwick et al., 2020). Nearly the entire sediment load is partitioned to delta-top aggradation, yielding a maximum aggradation rate and avulsion frequency limited by the sediment supply and lobe dimensions (Equation 6 for $D < 0$; black dashed line in Figure 10b). Shoreline retreat occurs across the delta—even at the active river mouth—and the avulsion node shifts upstream to maintain a constant avulsion length (Figure 6). During Phase D, avulsions ceased after 2 hr because the shoreline retreated to the confined-width river section of the flume (Figure 6d). However, Equation 6 suggests that had the river remained unconfined, avulsions would have continued and migrated farther upstream.

Experimental results show no significant change in the avulsion threshold with rise rate (Figure 10c). The dimensionless avulsion threshold, H^*, is within $0.1 - 1$ during Phase A (median $H^* = 0.5$ with 25–75 percentile range $[0.38 - 0.62]$), Phase B ($H^* = 0.30\,[0.21 - 0.44]$), Phase C ($H^* = 0.33\,[0.28 - 0.37]$), and Phase E ($H^* = 0.21\,[0.17 - 0.30]$). Measurements of avulsion threshold during phases D and F were not possible due to limited temporal resolution and spatial coverage of scan data. Overall results indicate that channels must aggrade to a height of $10 - 100\%$ the channel depth before avulsing regardless of sea-level conditions (Figure 10c). This range is consistent with existing theory and field data (Ganti et al., 2014; Jerolmack & Mohrig, 2007; Mohrig et al., 2000), with order-of-magnitude variability that is expected in part because the channel-filling model does not account for the avulsion trigger in each system (Kleinhans et al., 2013; Slingerland & Smith, 2004). Scatter in field data can be attributed in part to differing flood regimes: sites with more intense floods have a more pronounced triggering phase, and therefore require less channel aggradation between avulsions (Ganti et al., 2014). Both CROF16 and CROF18 featured the same amount of flood variability (the coefficient of variation of stage height is $CV = 1.62$ for both experiments), and both experiments featured a similar avulsion threshold ($H^* = 0.28\,[0.2 - 0.36]$ for CROF16, and $H^* = 0.29\,[0.2 - 0.38]$ for CROF18 across all phases).

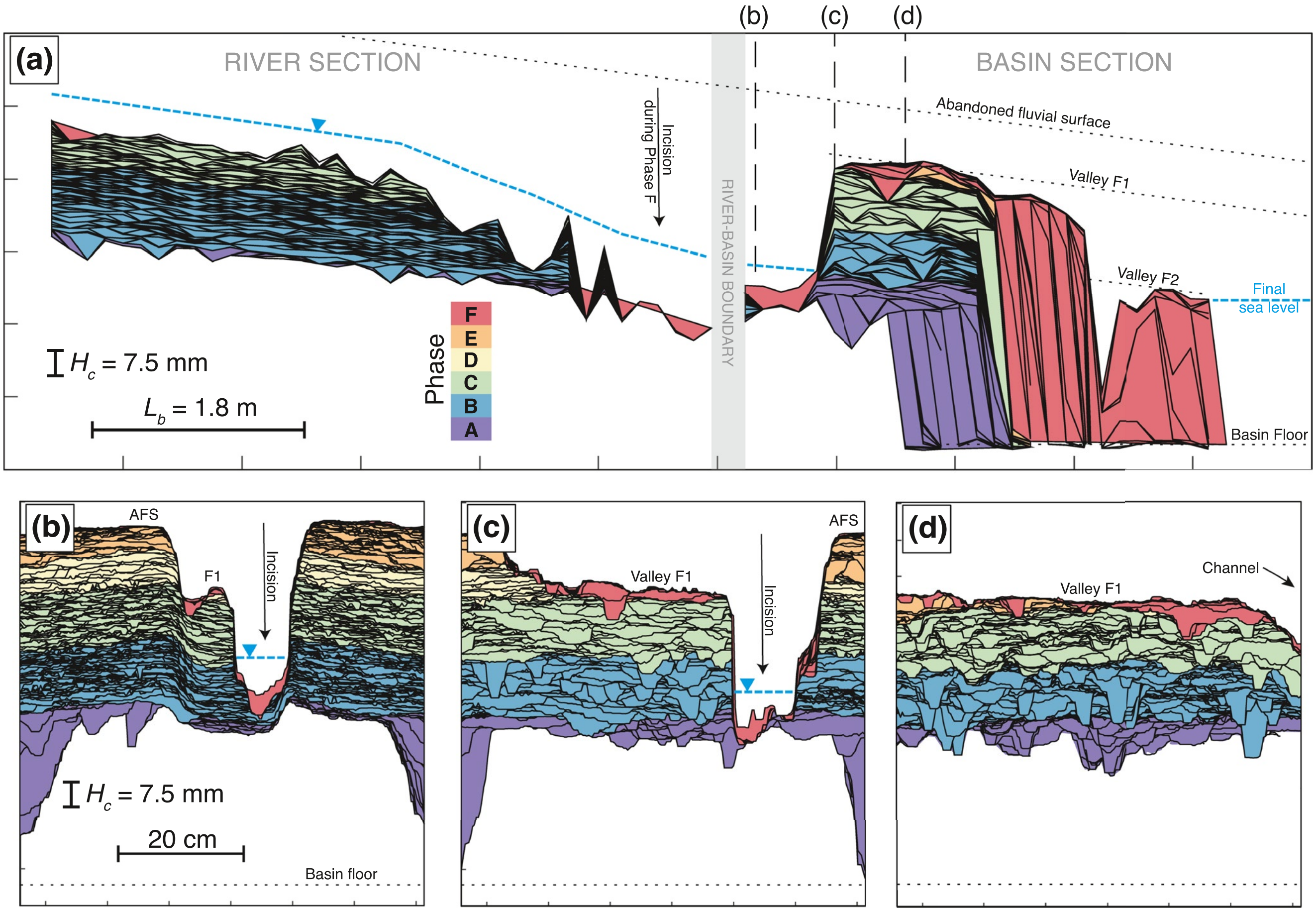

Figure 11. Synthetic stratigraphy of CROF18 in dip section (a) and three strike sections (b–d), showing scour surfaces (black lines) and depositional beds color-coded by experimental phase. Labels show elevation of the abandoned fluvial surface, Valley F1, Valley F2 and basin floor (dotted lines), approximate final water surface (blue dashed line), and incision during Phase F (downward arrow). Due to the orientation of the channel at the end of the experiment (Figure 8f), riverbed and water surface data are only available upstream of cross section (c).

3.3. Stratigraphic Signatures of Avulsions and Sea-Level Fall

Synthetic stratigraphy of CROF18 records distinct features associated with both avulsions and sea-level fall. A dip-section down the flume centerline shows that topset deposits from constant-sea-level and sea-level-fall conditions (phases A, E, and F) are primarily composed of foresets (Figure 11a). In contrast, deposits from sea-level-rise conditions (phases B–D) are dominated by topsets, consistent with previous studies (Martin et al., 2009; Yu et al., 2017). In the river section, individual beds are much thinner (Figure 11a) but show that deposition kept pace with delta-top aggradation to maintain a constant riverbed slope of 0.0042 (Table 1) (cf. Bijkerk et al., 2016; Mackin, 1948). By the end of Phase F, the channel incised more than 30 mm below the abandoned fluvial surface at the river-basin boundary, roughly $2.5L_b$ upstream of the river mouth (Figure 11a). Riverbed data downstream of this point are limited due to the configuration of the channel at the end of the experiment (Figure 8f), but the upstream riverbed featured a convex-up long profile characteristic of sea-level fall (Blum & Törnqvist, 2000; Schumm, 1993). Incision depth decreased upstream, down to only ~15 mm below the abandoned fluvial surface for reaches more than 3 m upstream the river-basin boundary (Figure 11a). Channel incision removed much of the deposit along the flume centerline, but beds bounded by scour surfaces are preserved in strike sections oriented perpendicular to the flume axis (Figures 11b–11d).

The thickness of preserved beds (Figures 11b–11d) primarily reflects the amount of aggradation between avulsions (Figure 12a). Downstream of the avulsion node, floods caused erosion that reduced the preserved bed thickness. Upstream of the avulsion node, avulsions caused scouring that reduce preserved bed thickness. However, near the avulsion node, aggradation rate was maximized and there was minimal erosion even during

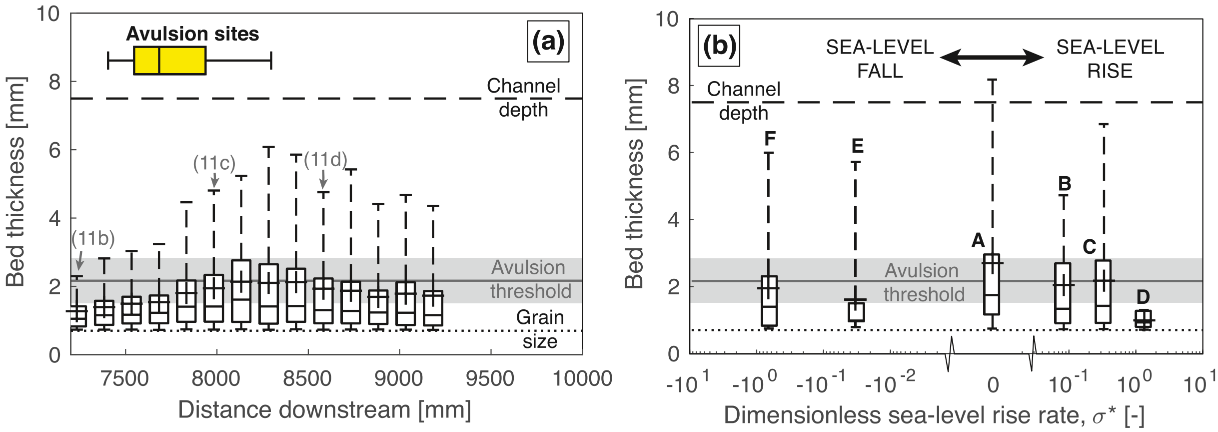

Figure 12. Bed thickness as a function of distance downstream (a) and dimensionless sea-level rise rate (b), showing channel depth (black dashed line), grain size (black dotted line), and avulsion threshold (gray line and shaded region corresponding to median and 25–75 percentile range of all avulsions). Box plots show median (horizontal bar), mean (plus sign), 25–75 percentile range (box), and 5–95 percentile range (whiskers). Yellow horizontal box plot in (a) shows distribution of all avulsion sites, and gray labels show location of cross sections in Figures 11b–11d. Bold labels in (b) denote experimental phases A–F. Visualization with logarithmic axes is provided in Figure S4 in Supporting Information S1.

floods, leading to greater preservation potential and a spatial maximum in bed thickness. Near the avulsion node (8,200–8,300 mm in Figure 12a), the average thickness of preserved beds (2.14 mm) reflects the amount of aggradation that occurred between avulsions ($H = 2.16$ mm on average), consistent with previous work (Ganti, Chadwick, Hassenruck-Gudipati, & Lamb, 2016; Mohrig et al., 2000). Greater preservation at the avulsion node is further supported by the observed natural variations in channel depth: channels were generally shallower near the avulsion node (e.g., Figure 3d) because scour there was minimal and aggradation was achieved through channel filling, which, in the absence of cohesive levee construction, necessarily reduced channel depths. Preserved beds were rarely thicker than the normal flow depth (7.5 mm; Figure 12a).

The bed-thickness distribution is similar regardless of rise rate (Figure 12b). Average bed thickness near the avulsion node reflects the same avulsion threshold under slow sea-level rise (Phase B), intermediate sea-level rise (Phase C), and even rapid sea-level fall (Phase F). Phases D and E are notable exceptions due to limited preservation; during Phase F, the channel scoured most of the sediment deposited during phases D–E (Figure 11a), resulting in thin beds. Thus, results indicate that bed-thickness distributions record the stratigraphic signature of avulsions regardless of rise rate, barring subsequent effects on preservation.

We identified two regimes in which scour depth preserves either the signature of avulsions or the signature of sea-level fall. If the height of cumulative sea-level drop Δz is less than the channel depth ($\Delta z < H_c$), then scour depth reflects incision during avulsions (Figure 13b). When the river changes course, it adjusts to its new, steeper path to the shoreline by incising the riverbed at the avulsion node and immediately upstream (Ganti et al., 2019). Avulsion-induced scour depths are highly variable and cluster around the avulsion threshold ($H = 2.17 \pm 0.65$ mm), with maximum values near the channel depth ($H_c = 7.5$ mm). Phase E provides an example of this regime: sea level fell slowly with a cumulative drop of only 3.5 mm (~50% of the channel depth; Figure 13a). As a result, the river continued to aggrade, and scours reflected erosion associated with avulsions rather than sea-level fall.

If the cumulative sea-level drop exceeds the channel depth ($\Delta z > H_c$), then scour depths fall in the second regime. In this regime the scour depth reflects the depth of sea-level fall, in agreement with sequence-stratigraphic models (cf. Allen & Posamentier, 1993; Van Wagoner, 1998). We document this behavior during Phase F, when sea level fell rapidly with a total drop of 47 mm (~630% of the channel depth), and the channel incised roughly at pace with sea-level fall (Figure 13a). During the first 10 hours of Phase F (140 − 150 hr), incision was slightly slower than sea-level fall because cumulative sea-level drop was not yet greater than the channel depth. Shortly after 150 hr, a pulse of incision associated with the abandonment of Valley F1 (Figures 8b and 8d) rendered the riverbed incision rate on par with sea level (Figure 13a). Thereafter, the channel continued to incise at pace with sea-level fall on average. Autogenic pulses in incision, aggradation, and avulsion distort the signal in this regime, but nevertheless we found $H_{scour} \sim \Delta z$ within a factor of two. We suspect the signal may grow further distorted when sea level is allowed to fall further beyond the scale of the basin depth (Figure 13b), because shallowing

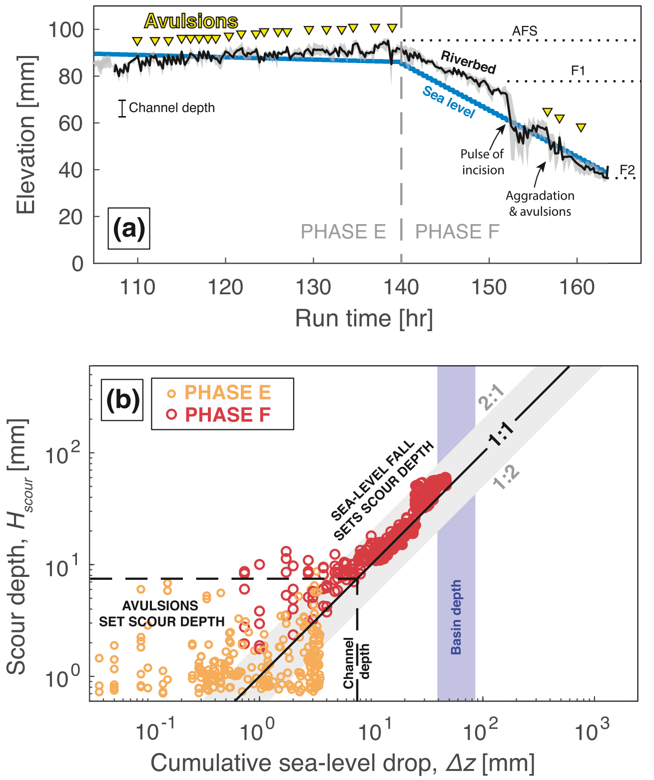

Figure 13. (a) Time series of riverbed elevation (black) and sea level (blue) during Phases E and F, showing avulsion events (yellow triangles), abandoned fluvial surface (black dashed line), and valleys F1 and F2 (black dotted lines). Riverbed is plotted as the spatial average (black) and range (gray shaded region) of the thalweg between cross sections of Figures 10b and 10c where data is available. (b) Scour depth H_{scour} as a function of sea-level drop Δz for phases E (orange) and F (red), showing trends of perfect agreement (black line) and agreement within a factor of two (gray shaded region). Scale of the channel depth (black dashed line) divides regimes where scour depth is set by avulsions and floods ($\Delta z < H_c$) or by sea-level fall ($\Delta z > H_c$). Blue shaded region shows range of basin depths during Phases E–F. Scour depth was measured as the relief between the riverbed and abandoned fluvial surface (for Phase F) or by the height of preserved sets between scour surfaces (for Phase E).

basin depths should allow for more rapid aggradation and avulsion (Carlson et al., 2018; Wang et al., 2019). Aggradation may also be facilitated by sediment redeposited from upstream incision (Blum & Törnqvist, 2000), but this was not a major factor for CROF18; we estimated that the river section of the flume would need to have been 10 times longer (50+ m, or 25+ backwater lengths) to yield enough sediment during incision to significantly affect delta aggradation rates.

4. Discussion

4.1. Comparison to Previous Work on Deltaic Avulsions

The CROF18 experiment provides the first documentation of a backwater-scaled experimental delta subjected to sea-level changes. We reproduced backwater-scaled avulsions in the laboratory by incorporating subcritical Froude numbers and variable flood discharges, similar to the earlier backwater-scaled experiment CROF16 (Ganti, Chadwick, Hassenruck-Gudipati, Fuller, & Lamb, 2016; Ganti, Chadwick, Hassenruck-Gudipati, & Lamb, 2016). Aggradation under constant sea-level conditions was caused by backfilling due to progradation, similar to previous experiments and models of low-sloping deltas (cf. Hoyal & Sheets, 2009; Moodie et al., 2019). Sea-level rise enhanced delta-top aggradation, resulting in more frequent avulsions, consistent with laboratory experiments and field observations (Martin et al., 2009; Stouthamer & Berendsen, 2001). Unlike constant-discharge experiments, CROF18 featured a variable flood regime that allowed persistent backwater effects to determine the avulsion length, leading to a scaling relationship between L_A and L_b similar to natural lowland deltas (Figure 10a; Figure 1c; Equation 1) (Ganti, Chadwick, Hassenruck-Gudipati, Fuller, & Lamb, 2016). In nature, many lowland deltas also feature prominent vegetation, cohesive floodplain deposition, and sediment reworking by waves and tides (Caldwell & Edmonds, 2014; Finotello et al., 2019; Nicholas et al., 2018). While these factors can influence avulsions (cf. Piliouras & Kim, 2019; Ratliff et al., 2021) in a manner not captured in our simplified experiment, CROF18 results nevertheless shed insight upon lowland delta avulsion dynamics. Subcritical flow conditions and a variable flood regime in CROF18 were sufficient to reproduce avulsion location and frequency trends consistent with field data for large lowland deltas, and show agreement with theoretical scaling relationships (Figure 10; Figure 1c). Consistency between simplified experiments and field data demonstrates that vegetation, cohesive sediment, and other factors are not necessary to reproduce backwater-scaled avulsion location and frequency patterns to first order.

CROF18 results support the notion that backwater-scaled avulsion nodes can originate from backwater hydrodynamics (Chadwick et al., 2019; Chatanantavet et al., 2012), even on deltas where backfilling is present (e.g., the Yellow River delta; Moodie et al., 2019; Zheng et al., 2019). Previously, backwater hydrodynamics and backfilling—the latter termed "morphodynamic backwater" by Hoyal and Sheets (2009)—have been viewed as competing hypotheses to explain how avulsions occur (cf. Brooke et al., 2020; Ratliff et al., 2021; Zheng et al., 2019). On the contrary, we find that these ideas are not in competition. When sea-level rise was slow or absent in CROF18, progradation and associated backfilling was the main driver of aggradation (Figures 3 and 4), consistent with past delta and fan experiments (de Haas et al., 2016; Hoyal & Sheets, 2009). At the same time, backwater hydrodynamics focused deposition in the upstream part of the backwater zone, leading to a preferential avulsion location that scaled with the backwater length (Figure 10a), consistent with backwater theory (Chadwick et al., 2019; Chatanantavet et al., 2012). When sea-level rise rate increased, aggradation was driven primarily by sea-level rise rather than progradation, and backwater effects continued to set the spatial maximum in aggradation rate and the preferential avulsion location (Figures 5–6, 10a). If backwater effects had not been incorporated

10.1029/2021JF006422

into the experiment, we expect that avulsion locations would have been random (Chadwick et al., 2019) or else governed by variations in levee and floodplain slope similar to earlier constant-discharge experiments (Edmonds et al., 2009; Ganti, Chadwick, Hassenruck-Gudipati, Fuller, & Lamb, 2016). A control experiment in the same flume without backwater effects but under otherwise similar conditions to CROF18 was conducted by Ganti, Chadwick, Hassenruck-Gudipati, Fuller, and Lamb (2016; Experiment A therein); their results showed that in the absence of backwater effects avulsions occurred repeatedly at the river-basin boundary, where there was an imposed abrupt increase in channel width that caused preferential deposition and avulsion. Modeling has shown that imposed changes in the channel width or floodplain slope, for example, due to rapid progradation or the arrangement of vegetation and biogenic sedimentation in coastal wetlands, can result in avulsion lengths that scale with the backwater length for geometric reasons even in the absence of persistent backwater hydrodynamics (Chadwick et al., 2019; Hoyal & Sheets, 2009; Prasojo et al., 2022; Ratliff et al., 2021). However, these geometric controls were not observed in our experiment.

The CROF18 experiment demonstrates lowland-delta avulsion nodes move basinward and landward in tandem with the shoreline during sea-level change. When shorelines prograded in CROF18, the avulsion node moved downstream to maintain a constant length between avulsions and the shoreline (Figures 3f, 4f and 10a). This behavior supports findings from the similarly scaled CROF16 experiment conducted under constant sea level (Ganti, Chadwick, Hassenruck-Gudipati, Fuller & Lamb, 2016), and observations on the Yellow River delta (Ganti et al., 2014). In CROF18, the avulsion node also moved landward during shoreline transgression, a behavior that has been predicted by numerical models (Chadwick et al., 2020; Ratliff et al., 2021) and recently identified in the Qaidam Basin, China (Li et al., 2022), but has never before been reproduced in the laboratory. In past experiments, hydraulic conditions were more analogous to experimental fans and fan deltas resulting in a geographically fixed avulsion location tied to flow expansion at the tank inlet (Ganti et al., 2014; Reitz & Jerolmack, 2012). In these cases, the avulsion node remains fixed even when sea-level rise causes shorelines to retreat; thus, the avulsion length (L_A) grows shorter and fan deltas and alluvial fans shrink in size (Jerolmack, 2009; Martin et al., 2009). Our results indicate lowland deltas respond differently: hydraulic backwater effects cause the avulsion node to move, resulting in a constant size (L_A) that scales with the backwater length (L_b), even during sea-level and shoreline change (Figure 10a).

The sediment mass-balance model of Equation 6 accurately estimates avulsion frequency in our experiment within uncertainty (Equation 6; Figure 10b). Based on reliable performance, we suggest this model could be applied to forecast avulsion hazards and be incorporated into land-loss projections for densely populated deltas in the next century. Experimental results also support Delft3D modeling of the Goose River delta (Nijhuis et al., 2015), showing avulsions may continue to occur during sea-level fall. Nijhuis et al. (2015) report higher sea-level fall rates are associated with more frequent avulsions, a trend observed in CROF18 due to shallow offshore basin depths (Figures 3f and Figures 7f–7g). In shallow basins, the river mouth is able to prograde rapidly, driving aggradation that can counteract sea-level fall and drive more frequent avulsion (Bijkerk et al., 2016; Wang et al., 2019). For deltas where the offshore basement is steep, progradation into deeper or shallower waters can also affect avulsion frequency (Carlson et al., 2018). While we did not explore this effect in CROF18, it can be incorporated into model predictions through the input basin-depth parameter H_b in Equation 6, as explored in Chadwick et al. (2020).

4.2. Implications for Predicting Avulsion Hazards

Our results indicate that the most likely site of future avulsion hazards is the location of maximum riverbed aggradation within the backwater zone (Figures 3c–3e, Figures 4c–4e, Figures 5c–5e, Figures 7c–7e). This finding supports the hypothesis of Chatanantavet et al. (2012) and is consistent with the earlier CROF16 experiment (Ganti, Chadwick, Hassenruck-Gudipati, Fuller, & Lamb, 2016) and estimates for natural deltas based on remote sensing (Brooke et al., 2020). Across a wide range of sea-level rise and fall conditions, our experiment produced a roughly constant avulsion length clustered within the backwater zone ($L_A < L_{b,bresse}$) and upstream of the zone of prominent scour ($L_A > L_{d,bresse}$) calculated using the Bresse solution (Equation 3). Thus, we suggest that past avulsion lengths on natural deltas are a good indicator of future avulsion lengths despite modern changes in relative sea level. To maintain a constant avulsion length during shoreline retreat, avulsion nodes are expected to move upstream, thereby introducing avulsion hazards farther inland than observed in recent history.

10.1029/2021JF006422

Avulsion-hazard-mitigation efforts may need to be expanded to new reaches upstream and should be prioritized on deltas where shorelines are retreating rapidly.

Our results also warn of increased frequency of avulsion hazards in the face of relative sea-level rise. As rise rates increase, so will aggradation rates. The avulsion threshold is expected to remain roughly constant for a given delta over a range of rise rates (Figure 10c), such that changes in aggradation rate will cause systematic changes in the avulsion frequency distribution (Figure 10b). On pristine deltas with limited anthropogenic modification, this will directly lead to more frequent avulsions farther upstream. We expect that imminent avulsions can be diagnosed based on a constant threshold amount of sedimentation, with a threshold between ∼10% and 100% of the channel depth (Figure 10c) that depends on flood regime (Ganti et al., 2014). Urbanized deltas are modified with artificial banks and levees to prevent avulsion (Syvitski & Saito, 2007), but could face avulsion hazards if this infrastructure is not maintained at pace with channel aggradation. More efforts, resources, and engineered diversions will be necessary to prevent avulsion as channels aggrade more quickly and farther upstream during sea-level rise (Kim et al., 2009; Moodie & Nittrouer, 2021; Temmerman & Kirwan, 2015). Modified deltas may also be at risk of unexpected new avulsion sites if levee and dam infrastructure has sufficiently altered backwater effects and aggradation patterns since the last avulsion (Carlson et al., 2021; Chadwick & Lamb, 2021; Moodie & Nittrouer, 2021).

4.3. Implications for Delta Stratigraphy During Sea-Level Fall

In conventional sequence-stratigraphic models, sea-level fall causes incision on deltas and the creation of incised valleys (Allen & Posamentier, 1993; Van Wagoner, 1998). Experimental results from CROF18 challenge this model, showing that significant aggradation and avulsion can continue during sea-level fall (Figure 13a). We found that aggradation and avulsions occur because rapid progradation counteracts incision if fall rates are relatively slow (Phase E) or if basin depths are relatively shallow (end of Phase F), consistent with recent work (Carlson et al., 2018; Chadwick et al., 2020; Wang et al., 2019). Other studies have proposed an alternative mechanism, wherein aggradation continues during sea-level fall because passive emergence of the continental shelf causes the shoreline to recede faster than the delta can prograde, thereby disconnecting the river system from base level until headward erosion from the shelf restores the connection (Van Heijst et al., 2001; Van Heijst & Postma, 2001). We did not observe this behavior in CROF18 because delta progradation was sufficient to keep pace with passive shoreline recession across the shelf. The backwater length of lowland deltas is often so large (often 100+ km; Table 3) that it rivals or surpasses the distance to the shelf edge (∼100–200 km along passive margins; Postma & Ziljstra, 1988). Because deltas typically prograde distances comparable to their backwater length between avulsions (Ganti et al., 2014), deltas with large backwater lengths are more capable of maintaining connection with base level as they prograde across the entire shelf edge. In sequence-stratigraphic terms, we expect this connection is maintained regardless of whether the delta is experiencing normal regression and associated topset aggradation (Phase E; Figure 7g) or forced regression and associated incision (Phase F; Figure 11a and Figure S2 in Supporting Information S1).

Where rapid sea-level fall does cause incision, scour depth does not necessarily reflect the drop in sea level. CROF18 results demonstrate scour depth accurately reflects sea-level fall only if the amount of sea-level drop is greater than the channel depth and also less than the basin depth ($H_c < \Delta z < H_b$) (Figure 13b). Any stratigraphic signal of smaller sea-level fall ($\Delta z \lesssim H_c$) is overprinted by scour during avulsions and floods, as hypothesized in earlier studies (Ganti et al., 2019; Trower et al., 2018). Even for higher rates of sea-level fall ($\Delta z \gtrsim H_b$), sea-level signals are distorted; deltaic rivers subject to steady sea-level fall cannot maintain a degradational state as the offshore basin shallows (Bijkerk et al., 2016; Chadwick et al., 2020) and will eventually transition to an aggradational state that reintroduces avulsions (Figure 13b). The window of sea-level-signal preservation ($H_c < \Delta z < H_b$) may be very narrow for large deltas, where channel depths (H_c) can be comparable to the depth of the continental shelf (H_b) (Edmonds et al., 2011).

Another interesting comparison between our experiment and sequence-stratigraphic models is in the formation of incised valleys. Multiple inset incised valleys would traditionally be interpreted to represent two distinct cycles of sea-level rise and fall, and channel infilling is commonly associated with episodes of sea-level rise (Allen & Posamentier, 1993; Van Wagoner, 1998; Zaitlin et al., 1994). However, CROF18 shows how coastal rivers can incise and fill nested valleys even under a constant rate of sea-level fall. During Phase F, two nested valleys formed because the channel incised while migrating gradually across the fluvial surface (Valley F1 and F2;

Figure 8; Figure 11). Fluvial surfaces less frequented by the channel eroded more slowly and were eventually abandoned when differential erosion left them perched above channel banks, consistent with earlier models and experiments of autogenic terrace formation (Limaye & Lamb, 2016; Muto & Steel, 2004). Valley F2 eventually infilled during sea-level fall because the offshore basin shallowed to allow more rapid progradation. Thus, Phase F demonstrates how the gradual migration of channels and shallowing of basin depth can significantly distort the amount of sea-level fall—and even the apparent number of sea-level cycles—preserved in the stratigraphy of incised valleys and valley fills.

5. Conclusions

We present results from a delta experiment scaled to incorporate backwater hydrodynamics and investigated river avulsion patterns and delta stratigraphy across a range of sea-level rise and fall rates. Across all sea-level conditions, avulsions occurred when and where the channel aggraded to a threshold height between 10% and 100% the channel depth. Aggradation rate was maximized within the backwater zone and upstream of the location of prominent scour during high flows, resulting in a preferential avulsion node set by the backwater length. Avulsion length was constant regardless of sea-level rise and fall; as a result, the avulsion node moved basinward during shoreline progradation, and moved landward during shoreline retreat. When sea level rose slowly ($\sigma^* < 0.1$), avulsion frequency was determined by the pace of delta progradation into the offshore basin. As sea-level rise rate increased, the river responded by avulsing more frequently. Avulsion-frequency response occurred across a critical regime of dimensionless rise rates ($0.1 < \sigma^* < 1$), corresponding to sea-level rise at a pace similar to but less than the maximum possible aggradation rate. When rise rate increased to exceed the maximum aggradation rate ($\sigma^* > 1$), avulsion frequency reached an upper limit set by sediment supply. Experimental results support recent model predictions for avulsion hazards on densely populated deltas in the next century (Figures 10a and 10b), and highlight that anthropogenic sea-level rise may induce more frequent avulsions farther inland than recorded previously.

Experimental results also demonstrate that sea-level fall does not necessarily inhibit river avulsions. River mouth progradation can counteract incision and drive repeated avulsions, provided sea-level fall is slow or the offshore basin is shallow. In the experimental delta stratigraphy, scour-bounded beds recorded the amount of aggradation between avulsions, suggesting that similar beds in the rock record provide a means to estimate paleo-avulsion thresholds (Mohrig et al., 2000). Channel avulsion and lateral migration drove pulses of autogenic incision, leading to the development of multiple incised valleys under steady sea-level fall. Preserved scour depths reflected the amount of sea-level fall, in support of sequence-stratigraphic models, but only when the cumulative drop in sea level is greater than the channel depth and also less than the basin depth ($H_c < \Delta z < H_b$; Figure 13). Outside of this window, sea-level signals are removed by avulsion-induced scours or distorted by progradation that counteracts incision. Results suggest that delta size affects how sea-level change is encoded in stratigraphy; sea-level-signal preservation may be especially limited for large deltas building into shallow basins.

Conflict of Interest

The authors declare no conflicts of interest relevant to this study.

Data Availability Statement

The data underlying this study are publicly available in the SEAD repository at http://doi.org/10.26009/s0FD85I6 (Chadwick, 2022). Analysis was performed and figures were made using MATLAB R2021b software available at www.mathworks.com (MATLAB, 2021).

Acknowledgments
We thank Brian Fuller, Tom Ulizio, and Kirby Sikes for assistance in conducting the experiment, and thank Maarten G. Kleinhans, Wonsuck Kim, and Katherine Ratliff for constructive reviews. We acknowledge NSF Grant EAR 1427262 and the Resnick Sustainability Institute at the California Institute of Technology for support.

References

Allen, G. P., & Posamentier, H. W. (1993). Sequence stratigraphy and facies model of an incised valley fill; the Gironde Estuary, France. *Journal of Sedimentary Research*, *63*(3), 378–391.

Arkesteijn, L., Blom, A., Czapiga, M. J., Chavarrías, V., & Labeur, R. J. (2019). The quasi-equilibrium longitudinal profile in backwater reaches of the engineered alluvial river: A space-marching method. *Journal of Geophysical Research: Earth Surface*, *124*(11), 2542–2560. https://doi.org/10.1029/2019JF005195

Aslan, A., Autin, W. J., & Blum, M. D. (2005). Causes of river avulsion: Insights from the late Holocene avulsion history of the Mississippi river, USA. *Journal of Sedimentary Research*, *75*(4), 650–664. https://doi.org/10.2110/jsr.2005.053

Bijkerk, J. F., Eggenhuisen, J. T., Kane, I. A., Meijer, N., Waters, C. N., Wignall, P. B., & McCaffrey, W. D. (2016). Fluvio-marine sediment partitioning as a function of basin water depth. *Journal of Sedimentary Research*, *86*(3), 217–235. https://doi.org/10.2110/jsr.2016.9

Bintanja, R., van de Wal, R. S. W., & Oerlemans, J. (2005). Modelled atmospheric temperatures and global sea levels over the past million years. *Nature*, *437*(7055), 125–128. https://doi.org/10.1038/nature03975

Blom, A., Arkesteijn, L., Chavarrías, V., & Viparelli, E. (2017). The equilibrium alluvial river under variable flow and its channel-forming discharge. *Journal of Geophysical Research: Earth Surface*, *122*(10), 1924–1948. https://doi.org/10.1002/2017jf004213

Blum, M. D., & Törnqvist, T. E. (2000). Fluvial responses to climate and sea-level change: A review and look forward. *Sedimentology*, *47*, 2–48. https://doi.org/10.1046/j.1365-3091.2000.00008.x

Bohacs, K., & Suter, J. (1997). Sequence stratigraphic distribution of coaly rocks: Fundamental controls and paralic examples. *AAPG Bulletin*, *81*(10), 1612–1639.

Brakenridge, G. R., Syvitski, J. P. M., Niebuhr, E., Overeem, I., Higgins, S. A., Kettner, A. J., & Prades, L. (2017). Design with nature: Causation and avoidance of catastrophic flooding, Myanmar. *Earth-Science Reviews*, *165*, 81–109. https://doi.org/10.1016/j.earscirev.2016.12.009

Bresse, J. A. C. (1860). *Cours de mecanique appliquee: 2: Hydraulique*. Mallet-Bachelier.

Brooke, S. A. S., Ganti, V., Chadwick, A. J., & Lamb, M. P. (2020). Flood variability determines the location of lobe-scale Avulsions on deltas: Madagascar. *Geophysical Research Letters*, *47*(20), e2020GL088797. https://doi.org/10.1029/2020gl088797

Bryant, M., Falk, P., & Paola, C. (1995). Experimental study of avulsion frequency and rate of deposition. *Geology*, *23*(4), 365. https://doi.org/10.1130/0091-7613(1995)023<0365:ESOAFA>2.3.CO;2

Caldwell, R. L., & Edmonds, D. A. (2014). The effects of sediment properties on deltaic processes and morphologies: A numerical modeling study. *Journal of Geophysical Research: Earth Surface*, *119*(5), 961–982. https://doi.org/10.1002/2013JF002965

Carlson, B. N., Nittrouer, J. A., Swanson, T. E., Moodie, A. J., Dong, T. Y., Ma, H., et al. (2021). Impacts of engineered diversions and natural avulsions on delta-lobe stability. *Geophysical Research Letters*, *48*(13), e2021GL092438. https://doi.org/10.1029/2021GL092438

Carlson, B. N., Piliouras, A., Muto, T., & Kim, W. (2018). Control of basin water depth on channel morphology and autogenic timescales in deltaic systems. *Journal of Sedimentary Research*, *88*(9), 1026–1039. https://doi.org/10.2110/jsr.2018.52

Chadwick, A. J. (2022). River avulsions and stratigraphy for an experimental lowland delta subjected to sea-level changes. SEAD Internal Repository. [Dataset] https://doi.org/10.26009/s0FD85I6

Chadwick, A. J., & Lamb, M. P. (2021). Climate-change controls on river delta avulsion location and frequency. *Journal of Geophysical Research: Earth Surface*, *126*(6), e2020JF005950. https://doi.org/10.1029/2020jf005950

Chadwick, A. J., Lamb, M. P., & Ganti, V. (2020). Accelerated river avulsion frequency on lowland deltas due to sea-level rise. *Proceedings of the National Academy of Sciences*, *117*(30), 17584–17590. https://doi.org/10.1073/pnas.1912351117

Chadwick, A. J., Lamb, M. P., Moodie, A. J., Parker, G., & Nittrouer, J. A. (2019). Origin of a preferential avulsion node on lowland river deltas. *Geophysical Research Letters*, *46*(8), 4267–4277. https://doi.org/10.1029/2019GL082491

Chamberlain, E. L., Törnqvist, T. E., Shen, Z., Mauz, B., & Wallinga, J. (2018). Anatomy of Mississippi Delta growth and its implications for coastal restoration. *Science Advances*, *4*(4), 1–10. https://doi.org/10.1126/sciadv.aar4740

Chatanantavet, P., & Lamb, M. P. (2014). Sediment transport and topographic evolution of a coupled river and river plume system: An experimental and numerical study. *Journal of Geophysical Research: Earth Surface*, *119*(6), 1–20. https://doi.org/10.1002/2013JF002810.Received

Chatanantavet, P., Lamb, M. P., & Nittrouer, J. A. (2012). Backwater controls of avulsion location on deltas. *Geophysical Research Letters*, *39*(1). https://doi.org/10.1029/2011GL050197

Coastal Protection and Restoration Authority of Louisiana. (2007). *Integrated ecosystem restoration and hurricane protection: Louisiana's comprehensive master plan for a sustainable coast*. State of Louisiana.

Coleman, J. M., Roberts, H. H., & Stone, G. W. (1998). Mississippi river delta: An overview. *Journal of Coastal Research*, *14*(3), 699–716.

de Haas, T., van den Berg, W., Braat, L., & Kleinhans, M. G. (2016). Autogenic avulsion, channelization and backfilling dynamics of debris-flow fans. *Sedimentology*, *63*(6), 1596–1619. https://doi.org/10.1111/sed.12275

Dunne, K. B. J., & Jerolmack, D. J. (2020). What sets river width? *Science Advances*, *6*(41), 1–9. https://doi.org/10.1126/sciadv.abc1505

Edmonds, D. A., Hoyal, D. C. J. D. C., Sheets, B. A., & Slingerland, R. L. (2009). Predicting delta avulsions: Implications for coastal wetland restoration. *Geology*, *37*(8), 759–762. https://doi.org/10.1130/G25743A.1

Edmonds, D. A., Shaw, J. B., & Mohrig, D. (2011). Topset-dominated deltas: A new model for River delta stratigraphy. *Geology*, *39*(12), 1175–1178. https://doi.org/10.1130/G32358.1

Farley, K. A., Williford, K. H., Stack, K. M., Bhartia, R., Chen, A., de la Torre, M., et al. (2020). Mars 2020 mission overview. *Space Science Reviews*, *216*(8), 1–41. https://doi.org/10.1007/s11214-020-00762-y

Finotello, A., Lentsch, N., & Paola, C. (2019). Experimental delta evolution in tidal environments: Morphologic response to relative sea-level rise and net deposition. *Earth Surface Processes and Landforms*, *44*(10), 2000–2015. https://doi.org/10.1002/esp.4627

Gagliano, S. M., Meyer-Arendt, K. J., & Wicker, K. M. (1981). Land loss in the Mississippi River deltaic plain. *GCAGS Transactions*, *31*, 295–300.

Ganti, V., Chadwick, A. J., Hassenruck-Gudipati, H. J., Fuller, B. M., & Lamb, M. P. (2016). Experimental river delta size set by multiple floods and backwater hydrodynamics. *Science Advances*, *2*(5), e1501768. https://doi.org/10.1126/sciadv.1501768

Ganti, V., Chadwick, A. J., Hassenruck-Gudipati, H. J., & Lamb, M. P. (2016). Avulsion cycles and their stratigraphic signature on an experimental backwater-controlled delta Vamsi. *Journal of Geophysical Research: Earth Surface*, *121*(9), 1–25. https://doi.org/10.1002/2016JF003915

Ganti, V., Chu, Z., Lamb, M. P., Nittrouer, J. A., & Parker, G. (2014). Testing morphodynamic controls on the location and frequency of river avulsions on fans versus deltas: Huanghe (Yellow River), China. *Geophysical Research Letters*, *41*(22), 7882–7890. https://doi.org/10.1002/2014GL061918

Ganti, V., Lamb, M. P., & Chadwick, A. J. (2019). Autogenic erosional surfaces in fluvio-deltaic stratigraphy from floods, avulsions, and backwater hydrodynamics. *Journal of Sedimentary Research*, *89*(8), 815–832. https://doi.org/10.2110/jsr.2019.40

Ganti, V., Paola, C., & Foufoula-Georgiou, E. (2013). Kinematic controls on the geometry of the preserved cross sets. *Journal of Geophysical Research: Earth Surface*, *118*(3), 1296–1307. https://doi.org/10.1002/jgrf.20094

Ganti, V., Straub, K. M., Foufoula-Georgiou, E., & Paola, C. (2011). Space-time dynamics of depositional systems: Experimental evidence and theoretical modeling of heavy-tailed statistics. *Journal of Geophysical Research*, *116*(F2). https://doi.org/10.1029/2010jf001893

Giosan, L., Donnelly, J. P., Constantinescu, S., Filip, F., Ovejanu, I., Vespremeanu-Stroe, A., et al. (2006). Young Danube delta documents stable Black Sea level since the middle Holocene: Morphodynamic, paleogeographic, and archaeological implications. *Geology*, *34*(9), 757–760. https://doi.org/10.1130/G22587.1

Gleick, P. H. (2003). Global freshwater resources: Soft-path solutions for the 21st century. *Science*, *302*(5650), 1524–1528. https://doi.org/10.1126/science.1089967

González, J. L., & Tornqvist, T. E. (2006). Coastal Louisiana in crisis: Subsidence or sea level rise? *Eos, Transactions American Geophysical Union*, *87*(45), 493–498. https://doi.org/10.1029/2006eo450001

Hajek, E. A., & Straub, K. M. (2017). Autogenic sedimentation in clastic stratigraphy. *Annual Review of Earth and Planetary Sciences*, *45*(1), 681–709. https://doi.org/10.1146/annurev-earth-063016-015935

Hajek, E. A., & Wolinsky, M. A. (2012). Simplified process modeling of river avulsion and alluvial architecture: Connecting models and field data. *Sedimentary Geology*, *257–260*, 1–30. https://doi.org/10.1016/j.sedgeo.2011.09.005

Hariharan, J., Xu, Z., Michael, H. A., Paola, C., Steel, E., & Passalacqua, P. (2021). Linking the surface and subsurface in river deltas—Part 1: Relating surface and subsurface geometries. *Water Resources Research*, *57*(8), e2020WR029282.

Hayden, A. T., Lamb, M. P., Fischer, W. W., Ewing, R. C., McElroy, B. J., & Williams, R. M. E. (2019). Formation of sinuous ridges by inversion of river-channel belts in Utah, USA, with implications for Mars. *Icarus*, *332*, 92–110. https://doi.org/10.1016/j.icarus.2019.04.019

Hoyal, D., & Sheets, B. A. (2009). Morphodynamic evolution of experimental cohesive deltas. *Journal of Geophysical Research*, *114*(F2), F02009. https://doi.org/10.1029/2007JF000882

Jelgersma, S. (1996). Land subsidence in coastal lowlands. In *sea-level rise and coastal subsidence* (pp. 47–62). Springer.

Jerolmack, D. J. (2009). Conceptual framework for assessing the response of delta channel networks to Holocene sea level rise. *Quaternary Science Reviews*, *28*(17–18), 1786–1800. https://doi.org/10.1016/j.quascirev.2009.02.015

Jerolmack, D. J., & Mohrig, D. (2007). Conditions for branching in depositional rivers. *Geology*, *35*(5), 463. https://doi.org/10.1130/G23308A.1

Jerolmack, D. J., & Swenson, J. B. (2007). Scaling relationships and evolution of distributary networks on wave-influenced deltas. *Geophysical Research Letters*, *34*(23). https://doi.org/10.1029/2007GL031823

Kidder, T. R., & Liu, H. (2017). Bridging theoretical gaps in geoarchaeology: Archaeology, geoarchaeology, and history in the Yellow River valley, China. *Archaeological and Anthropological Sciences*, *9*(8), 1585–1602. https://doi.org/10.1007/s12520-014-0184-5

Kim, W., Mohrig, D., Twilley, R. R., Paola, C., & Parker, G. (2009). Is it feasible to build new land in the Mississippi River delta? *Eos Transactions, AGU*, *90*(42), 373–374. https://doi.org/10.1029/2009eo420001

Kleinhans, M. G. (2010). Sorting out river channel patterns. *Progress in Physical Geography*, *34*(3), 287–326. https://doi.org/10.1177/0309133310365300

Kleinhans, M. G., Braudrick, C., van Dijk, W. M., de Lageweg, W. I., Teske, R., & Van Oorschot, M. (2015). Swiftness of biomorphodynamics in Lilliput-to Giant-sized rivers and deltas. *Geomorphology*, *244*, 56–73. https://doi.org/10.1016/j.geomorph.2015.04.022

Kleinhans, M. G., Ferguson, R. I., Lane, S. N., & Hardy, R. J. (2013). Splitting rivers at their seams: Bifurcations and avulsion. *Earth Surface Processes and Landforms*, *38*(1), 47–61. https://doi.org/10.1002/esp.3268

Kleinhans, M. G., Leuven, J. R. F. W., Braat, L., & Baar, A. (2017). Scour holes and ripples occur below the hydraulic smooth to rough transition of movable beds. *Sedimentology*, *64*(5), 1381–1401. https://doi.org/10.1111/sed.12358

Kleinhans, M. G., van Dijk, W. M., van de Lageweg, W. I., Hoyal, D. C. J. D., Markies, H., van Maarseveen, M., et al. (2014). Quantifiable effectiveness of experimental scaling of river-and delta morphodynamics and stratigraphy. *Earth-Science Reviews*, *133*, 43–61. https://doi.org/10.1016/j.earscirev.2014.03.001

Lamb, M. P., Nittrouer, J. A., Mohrig, D., & Shaw, J. (2012). Backwater and river plume controls on scour upstream of river mouths: Implications for fluvio-deltaic morphodynamics. *Journal of Geophysical Research*, *117*(F1), F01002. https://doi.org/10.1029/2011JF002079

Lane, T. I., Nanson, R. A., Vakarelov, B. K., Ainsworth, R. B., & Dashtgard, S. E. (2017). *Evolution and architectural styles of a forced-regressive Holocene delta and megafan, Mitchell River, Gulf of Carpentaria, Australia T* (Vol. 444). Geological Society of London, Special Publications.

Li, J., Ganti, V., Li, C., & Wei, H. (2022). Upstream migration of avulsion sites on lowland deltas with river-mouth retreat. *Earth and Planetary Science Letters*, *577*, 117270. https://doi.org/10.1016/j.epsl.2021.117270

Li, Q., Yu, L., & Straub, K. M. (2016). Storage thresholds for relative sea-level signals in the stratigraphic record. *Geology*, *44*(3), 179–182. https://doi.org/10.1130/g37484.1

Limaye, A. B. S., & Lamb, M. P. (2016). Numerical model predictions of autogenic fluvial terraces and comparison to climate change expectations. *Journal of Geophysical Research: Earth Surface*, *121*(3), 512–544. https://doi.org/10.1002/2014jf003392

Mackin, J. H. (1948). Concept of the graded river. *The Geological Society of America Bulletin*, *59*(5), 463–512. https://doi.org/10.1130/0016-7606(1948)59[463:cotgr]2.0.co;2

Malatesta, L. C., Prancevic, J. P., & Avouac, J.-P. (2017). Autogenic entrenchment patterns and terraces due to coupling with lateral erosion in incising alluvial channels. *Journal of Geophysical Research: Earth Surface*, *122*(1), 335–355. https://doi.org/10.1002/2015jf003797

Martin, J., Sheets, B., Paola, C., & Hoyal, D. (2009). Influence of steady base-level rise on channel mobility, shoreline migration, and scaling properties of a cohesive experimental delta. *Journal of Geophysical Research*, *114*(F3), F03017. https://doi.org/10.1029/2008JF001142

MATLAB. (2021). 9.11.0.1769968(R2021b). Natick, Masachusetts: The Mathworks Inc. [Software].

Milliman, J. D., Broadus, J. M., & Gable, F. (1989). Environmental and economic implications of rising sea level and subsiding deltas: The Nile and Bengal examples. *Ambio*, 340–345.

Milliman, J. D., & Syvitski, J. P. M. (1992). Geomorphic/Tectonic control of sediment discharge to the ocean: The importance of small mountainous rivers. *The Journal of Geology*, *100*(5), 525–544. https://doi.org/10.1086/629606

Mohrig, D., Heller, P. L., & Lyons, W. J. (2000). Interpreting avulsion process from ancient alluvial sequences: Guadalope-Matarranya system (northern Spain) and Wasatch Formation (western Colorado). *Geological Society of America Bulletin*, *112*(12), 1787–1803.

Moodie, A. J., & Nittrouer, J. A. (2021). Optimized river diversion scenarios promote sustainability of urbanized deltas. *Proceedings of the National Academy of Sciences*, *118*(27). https://doi.org/10.1073/pnas.2101649118

Moodie, A. J., Nittrouer, J. A., Ma, H., Carlson, B. N., Chadwick, A. J., Lamb, M. P., & Parker, G. (2019). Modeling deltaic lobe-building cycles and channel avulsions for the Yellow River delta, China. *Journal of Geophysical Research: Earth Surface*, *124*(11), 2438–2462. https://doi.org/10.1029/2019JF005220

Moran, K. E., Nittrouer, J. A., Perillo, M. M., Lorenzo-Trueba, J., & Anderson, J. B. (2017). Morphodynamic modeling of fluvial channel fill and avulsion time scales during early Holocene transgression, as substantiated by the incised valley stratigraphy of the Trinity River, Texas. *Journal of Geophysical Research: Earth Surface*, *122*(1), 215–234. https://doi.org/10.1002/2015JF003778

Muto, T., & Steel, R. J. (2004). Autogenic response of fluvial deltas to steady sea-level fall: Implications from flume-tank experiments. *Geology*, *32*(5), 401–404. https://doi.org/10.1130/G20269.1

Nicholas, A. P., Aalto, R. E., Smith, G. H. S., & Schwendel, A. C. (2018). Hydrodynamic controls on alluvial ridge construction and avulsion likelihood in meandering river floodplains. *Geology*, *46*(7), 639–642. https://doi.org/10.1130/g40104.1

Nijhuis, A. G., Edmonds, D. A., Caldwell, R. L., Cederberg, J. A., Slingerland, R. L., Best, J. L., et al. (2015). Fluvio-deltaic avulsions during relative sea-level fall. *Geology*, *43*(8), 719–722. https://doi.org/10.1130/g36788.1

Olson, D. M., & Dinerstein, E. (1998). The global 200: A representation approach to conserving the earth's most biologically valuable ecoregions. *Conservation Biology*, *12*(3), 502–515. https://doi.org/10.1046/j.1523-1739.1998.012003502.x

Pachauri, R. K., Allen, M. R., Barros, V. R., Broome, J., Cramer, W., Christ, R., et al. (2014). Climate change 2014: Synthesis report. In R. Pachauri & L. Meyer (Eds.), *Contribution of working groups I, II and III to the fifth assessment report of the Intergovernmental Panel on Climate Change* (p. 151). IPCC.

Pang, J., & Si, S. (1979). The estuary changes of Huanghe river I. Changes in modern time. *Oceanologia et Limnologia Sinica*, *2*.

Paola, C., Ganti, V., Mohrig, D., Runkel, A. C., & Straub, K. M. (2018). Time not our time: Physical controls on the preservation and measurement of geologic time. *Annual Review of Earth and Planetary Sciences*, *46*(1), 409–438. https://doi.org/10.1146/annurev-earth-082517-010129

Paola, C., & Mohrig, D. (1996). Palaeohydraulics revisited: Palaeoslope estimation in coarse-grained braided rivers. *Basin Research*, *8*(3), 243–254. https://doi.org/10.1046/j.1365-2117.1996.00253.x

Paola, C., Straub, K., Mohrig, D., & Reinhardt, L. (2009). The "unreasonable effectiveness" of stratigraphic and geomorphic experiments. *Earth-Science Reviews*, *97*(1–4), 1–43. https://doi.org/10.1016/j.earscirev.2009.05.003

Parker, G., Muto, T., Akamatsu, Y., Dietrich, W. E., & Lauer, J. W. (2008). Unravelling the conundrum of river response to rising sea-level from laboratory to field. Part II. The Fly-Strickland River system, Papua New Guinea. *Sedimentology*, *55*(6), 1657–1686. https://doi.org/10.1111/j.1365-3091.2008.00962.x

Pelletier, J. D., & DeLong, S. (2004). Oscillations in arid alluvial-channel geometry. *Geology*, *32*(8), 713–716. https://doi.org/10.1130/g20512.1

Pierik, H. J., Stouthamer, E., & Cohen, K. M. (2017). Natural levee evolution in the Rhine-Meuse delta, The Netherlands, during the first millennium CE. *Geomorphology*, *295*, 215–234. https://doi.org/10.1016/j.geomorph.2017.07.003

Piliouras, A., & Kim, W. (2019). Delta size and plant patchiness as controls on channel network organization in experimental deltas. *Earth Surface Processes and Landforms*, *44*(1), 259–272. https://doi.org/10.1002/esp.4492

Postma, H. (1988). Continental shelves. In J. J. Zijlstra (Ed.), *Ecosystems of the world* (Vol. 27, p. 421). Elsevier Science Publisher.

Prasojo, O. A., Hoey, T. B., Owen, A., & Williams, R. D. (2022). Slope break and avulsion locations scale consistently in global deltas. *Geophysical Research Letters*, *49*(2), e2021GL093656. https://doi.org/10.1029/2021gl093656

Ratliff, K. M., Hutton, E. H. W., & Murray, A. B. (2018). Exploring wave and sea-level rise effects on delta morphodynamics with a coupled River-Ocean model. *Journal of Geophysical Research: Earth Surface*, *123*(11), 2887–2900. https://doi.org/10.1029/2018JF004757

Ratliff, K. M., Hutton, E. W. H., & Murray, A. B. (2021). Modeling long-term delta dynamics reveals persistent geometric river avulsion locations. *Earth and Planetary Science Letters*, *559*, 116786. https://doi.org/10.1016/j.epsl.2021.116786

Reitz, M. D., & Jerolmack, D. J. (2012). Experimental alluvial fan evolution: Channel dynamics, slope controls, and shoreline growth. *Journal of Geophysical Research*, *117*(F2), F02021. https://doi.org/10.1029/2011JF002261

Reitz, M. D., Jerolmack, D. J., & Swenson, J. B. (2010). Flooding and flow path selection on alluvial fans and deltas. *Geophysical Research Letters*, *37*(6). https://doi.org/10.1029/2009GL041985

Reitz, M. D., Pickering, J. L., Goodbred, S. L., Paola, C., Steckler, M. S., Seeber, L., & Akhter, S. H. (2015). Effects of tectonic deformation and sea level on River path selection: Theory and application to the ganges-brahmaputra-meghna river delta. *Journal of Geophysical Research: Earth Surface*, *120*(4), 671–689. https://doi.org/10.1002/2014JF003202

Richards, K., Brasington, J., & Hughes, F. (2002). Geomorphic dynamics of floodplains: Ecological implications and a potential modelling strategy. *Freshwater Biology*, *47*(4), 559–579. https://doi.org/10.1046/j.1365-2427.2002.00920.x

Salter, G., Paola, C., & Voller, V. R. (2018). Control of delta avulsion by downstream sediment sinks. *Journal of Geophysical Research: Earth Surface*, *123*(1), 142–166. https://doi.org/10.1002/2017JF004350

Schumm, S. A. (1993). River response to baselevel change: Implications for sequence stratigraphy. *The Journal of Geology*, *101*(2), 279–294. https://doi.org/10.1086/648221

Shaw, J. B., & McElroy, B. (2016). Backwater number scaling of alluvial bed forms. *Journal of Geophysical Research: Earth Surface*, *121*(8), 1436–1455. https://doi.org/10.1002/2016jf003861

Sinha, R. (2009). The great avulsion of Kosi on 18 August 2008. *Current Science*, 429–433.

Slingerland, R., & Smith, N. D. (1998). Necessary conditions for a meandering-river avulsion. *Geology*, *26*(5), 435–438. https://doi.org/10.1130/0091-7613(1998)026<0435:NCFAMR>2.3.CO;2

Slingerland, R., & Smith, N. D. (2004). river avulsions and their deposits. *Annual Review of Earth and Planetary Sciences*, *32*(1), 257–285. https://doi.org/10.1146/annurev.earth.32.101802.120201

Soong, T. W., & Zhao, Y. (1994). The flood and sediment characteristics of the Lower Yellow River in China. *Water International*, *19*(3), 129–137. https://doi.org/10.1080/02508069408686216

Stouthamer, E., & Berendsen, H. J. A. (2000). Factors controlling the Holocene avulsion history of the Rhine-Meuse delta (The Netherlands). *Journal of Sedimentary Research*, *70*(5), 1051–1064. https://doi.org/10.1306/033000701051

Stouthamer, E., & Berendsen, H. J. A. (2001). Avulsion frequency, avulsion duration, and interavulsion period of Holocene channel belts in the rhine-meuse delta, The Netherlands. *Journal of Sedimentary Research*, *71*(4), 589–598. https://doi.org/10.1306/112100710589

Straub, K. M., Ganti, V., Paola, C., & Foufoula-Georgiou, E. (2012). Prevalence of exponential bed thickness distributions in the stratigraphic record: Experiments and theory. *Journal of Geophysical Research*, *117*(F2). https://doi.org/10.1029/2011jf002034

Syvitski, J. P. M. (2008). Deltas at risk. *Sustainability Science*, *3*(1), 23–32. https://doi.org/10.1007/s11625-008-0043-3

Syvitski, J. P. M., & Brakenridge, G. R. (2013). Causation and avoidance of catastrophic flooding along the Indus River, Pakistan. *Geological Society of America Today*, *23*(1), 4–10. https://doi.org/10.1130/gsatg165a.1

Syvitski, J. P. M., & Saito, Y. (2007). Morphodynamics of deltas under the influence of humans. *Global and Planetary Change*, *57*(3–4), 261–282. https://doi.org/10.1016/j.gloplacha.2006.12.001

Tal, M., & Paola, C. (2007). Dynamic single-thread channels maintained by the interaction of flow and vegetation. *Geology*, *35*(4), 347–350. https://doi.org/10.1130/G23260A.1

Temmerman, S., & Kirwan, M. L. (2015). Building land with a rising sea. *Science*, *349*(6248), 588–589. https://doi.org/10.1126/science.aac8312

Törnqvist, T. E., Wallace, D. J., Storms, J. E. A., Wallinga, J., Van Dam, R. L., Blaauw, M., et al. (2008). Mississippi Delta subsidence primarily caused by compaction of Holocene strata. *Nature Geoscience*, *1*(3), 173–176. https://doi.org/10.1038/ngeo129

Trower, E. J., Ganti, V., Fischer, W. W., & Lamb, M. P. (2018). Erosional surfaces in the Upper Cretaceous Castlegate Sandstone (Utah, USA): Sequence boundaries or autogenic scour from backwater hydrodynamics? *Geology*, *46*(8), 707–710. https://doi.org/10.1130/g40273.1

Van Dijk, M., Kleinhans, M. G., Postma, G., & Kraal, E. (2012). Contrasting morphodynamics in alluvial fans and fan deltas: Effect of the downstream boundary. *Sedimentology*, *59*(7), 2125–2145. https://doi.org/10.1111/j.1365-3091.2012.01337.x

Van Heijst, M. W. I. M., & Postma, G. (2001). Fluvial response to sea-level changes: A quantitative analogue, experimental approach. *Basin Research*, *13*(3), 269–292. https://doi.org/10.1046/j.1365-2117.2001.00149.x

Van Heijst, M. W. I. M., Postma, G., Meijer, X. D., Snow, J. N., & Anderson, J. B. (2001). Quantitative analogue flume-model study of river-shelf systems: Principles and verification exemplified by the late Quaternary Colorado river-delta evolution. *Basin Research*, *13*(3), 243–268. https://doi.org/10.1046/j.1365-2117.2001.00150.x

Van Wagoner, J. C. (1998). Sequence stratigraphy and marine to nonmarine facies architecture of foreland basin strata, book cliffs, Utah, USA: Reply. *AAPG Bulletin*, *82*(8), 1607–1618.

Vörösmarty, C. J., Syvitski, J., Day, J., de Sherbinin, A., Giosan, L., & Paola, C. (2009). Battling to save the world's river deltas. *Bulletin of the Atomic Scientists*, *65*(2), 31–43. https://doi.org/10.2968/065002005

Wang, J., Muto, T., Urata, K., Sato, T., & Naruse, H. (2019). Morphodynamics of river deltas in response to different basin water depths: An experimental examination of the grade index model. *Geophysical Research Letters*, *46*(10), 5265–5273. https://doi.org/10.1029/2019gl082483

Wickert, A. D., Martin, J. M., Tal, M., Kim, W., Sheets, B., & Paola, C. (2013). River channel lateral mobility: Metrics, time scales, and controls. *Journal of Geophysical Research: Earth Surface*, *118*(2), 396–412. https://doi.org/10.1029/2012JF002386

Wu, C., & Nitterour, J. A. (2020). Impacts of backwater hydrodynamics on fluvial–deltaic stratigraphy. *Basin Research*, *32*(3), 567–584. https://doi.org/10.1111/bre.12385

Yu, L., Li, Q., & Straub, K. M. (2017). Scaling the response of deltas to relative-Sea-level cycles by autogenic space and time scales: A laboratory study. *Journal of Sedimentary Research*, *87*(8), 817–837. https://doi.org/10.2110/jsr.2017.46

Yu, S.-Y., Törnqvist, T. E., & Hu, P. (2012). Quantifying Holocene lithospheric subsidence rates underneath the Mississippi Delta. *Earth and Planetary Science Letters*, *331*, 21–30. https://doi.org/10.1016/j.epsl.2012.02.021

Zaitlin, B. A., Dalrymple, R. W., & Boyd, R. (1994). The stratigraphic organization of incised-valley systems associated with relative sea-level change. In *Incised-valley systems: Origin and sedimentary sequences* (Vol. 51). SEPM Society for Sedimentary Geology. https://doi.org/10.2110/pec.94.12.0045

Zheng, S., Edmonds, D. A., Wu, B., & Han, S. (2019). Backwater controls on the evolution and avulsion of the qingshuigou channel on the Yellow River delta. *Geomorphology*, *333*, 137–151. https://doi.org/10.1016/j.geomorph.2019.02.032